10-8-2013 12:00 AM

Dynamic Light Scattering Study of Hydroxyapatite Formation: Effect of Osteopontin and Bone Sialoprotein

Maryam Mozaffari
The University of Western Ontario

Supervisor
Profs. John R. de Bruyn
The University of Western Ontario Joint Supervisor
Harvey A. Goldberg
The University of Western Ontario

Graduate Program in Physics
A thesis submitted in partial fulfillment of the requirements for the degree in Master of Science

Recommended Citation

Mozaffari, Maryam, "Dynamic Light Scattering Study of Hydroxyapatite Formation: Effect of Osteopontin and Bone Sialoprotein" (2013). *Electronic Thesis and Dissertation Repository*. 1660.
https://ir.lib.uwo.ca/etd/1660

Dynamic Light Scattering Study of Hydroxyapatite Formation: Effect of Osteopontin and Bone Sialoprotein

(Thesis format: Monograph)

by

Maryam Mozaffari

Graduate Program in Physics

A thesis submitted in partial fulfillment
of the requirements for the degree of
Master of Science

The School of Graduate and Postdoctoral Studies
The University of Western Ontario
London, Ontario, Canada

Abstract

Biomineralization is the process by which living organisms synthesize minerals. Some bone-related proteins, such as bone sialoprotein (BSP), have been found to enhance biomineralization, while others, including osteopontin (OPN), act as inhibitors of this process. Dynamic light scattering was used to investigate the effect of several native and recombinant proteins and peptides on the formation and growth of hydroxyapatite (HA) crystals from solutions of Ca^{2+} and PO_4^{3-} ions. We studied two isoforms of OPN, the OPN-derived peptides P0, P3, OPAR and pOPAR, and recombinant BSP. X-ray diffraction was used to identify the precipitate as HA crystals. Native OPN inhibits the nucleation of HA crystals, while recombinant OPN strongly inhibits their growth. Among the peptides studied, the non-phosphorylated P0 weakly inhibits HA growth, while P3, which has three phosphates, is a potent inhibitor of HA nucleation. OPAR is found to moderately inhibit nucleation, while its phosphorylated isoform pOPAR more strongly inhibits the nucleation of the HA crystals as well as having a small effect on their growth. This work confirms that phosphorylation of OPN is essential to its capability to prevent mineral growth. Our results show that for high enough ion and protein concentrations, rBSP inhibits the nucleation of HA, while there is some evidence that it enhances nucleation at very low protein concentrations

.

Acknowledgments

First, I must express my sincere gratitude to my advisors, Profs. John de Bruyn and Harvey Goldberg, for their endless support and guidance in supervising my Master's research. I appreciate their patience with my own sometimes erratic style and pace in scientific work. I also want to thank them for instilling a friendly and cooperative atmosphere in their labs. It was a great pleasure to work with them.

I am especially indebted to Prof. Graeme Hunter for his contribution to my understanding of this subject matter.

I am thankful to Prof. Roberta Flemming and Michael Bramble for their assistance in performing the XRD measurements.

I would especially like to thank Yinyin Liao, Honghong Chen, and Dr. Bernd Grohe, who helped a lot with the work presented in this dissertation.

I am thankful to all members of our research group, especially Masha and Erik, for their useful helps and the great discussions we had in our group meetings.

And last, but certainly not least, I would like to thank my parents and my sister for their encouragement and love and for setting a perfect example for me as thoughtful and caring human beings, which I have tried to follow.

Contents

List of Tables

List of Figures

Chapter 1: Introduction and Literature Review

1.1 Biomineralization

Living organisms are capable of controlling the nucleation, growth and morphology of inorganic crystals within mineralized tissue. This process is called biomineralization. The geological record indicates that biomineralization has existed in some form for 3.5 billion years and that skeletal development first took place during Cambrian explosion [1]. Biomineralization occurs not only in the five animal kingdoms [2] but also in many plant species. Mollusk shells consist of two kinds of calcium carbonate ($CaCO_3$), argonite and calcite [3]. Hydroxyapatite ($Ca_{10}(PO_4)_6(OH)_2$) is the major mineral component of mammalian bones and teeth and it makes up approximately 65% of their structure by weight [4], while plants are able to synthesize minerals such as calcium oxalate (CaC_2O_4) within their roots, leaves, stems and flowers as well as in fruits and seeds [5,6,7].

Minerals that have been made biologically contain organic as well as mineral components. They are produced under unusual conditions that are far from equilibrium, so the size, shape and crystallinity of biominerals are often very different from those of equivalent minerals formed by abiotic processes [5,8].

Precise biochemical balancing of the biomineralization mechanism by protein inhibitors or nucleators is needed to prevent ectopic calcification or undesired mineral formation in soft tissues. Biological fluids like blood and urine are supersaturated with a variety of mineral salts, but regulatory proteins and low molecular weight inhibitors like citrate and pyrophosphate are responsible for preventing the minerals from coming out of solution [9]. A deficiency of the appropriate inhibitors of biominerals can lead to precipitation, resulting in pathological deposition such as arterial plaque and kidney stone [10].

Bone is a type of rigid connective tissue which serves to provide mechanical support for the body and to protect some organs, including the brain and spinal cord. Bone plays a role in the regulation of Ca^{2+} and PO_4^{3-} ions in the body because it is a reservoir of these ions [11]. Cells in the bone, including osteoblasts, osteocytes and osteoclasts have responsibility for remodeling the extracellular matrix (ECM), which provides structural support and is important for maintaining bone health. The organic extracellular matrix of bone consists of 90% type I collagen, while the remainder is non-collagenous proteins such as bone sialoprotein (BSP) and osteopontin (OPN). Type I collagen acts as a scaffold for the tissue, whereas the non-collagenous proteins, including the members of the SIBLING family of proteins discussed in Section 1.3, are responsible for the modulation of crystal nucleation, growth and orientation [12]. Hydroxyapatite that is formed on this scaffold is oriented along the long axis of the collagen fibers. It exists in bone and teeth as well as in pathological calcifications such as kidney stones and arterial plaque. Abiotic hydroxyapatite can be found in the form of a monoclinic crystal prism and hexagonal crystals at temperatures below and above 250°C respectively, while biological HA forms hexagonal crystals [13].

1.2 Crystal Nucleation and Growth

Many biomineral products precipitate from an initial solution phase and are either completely crystalline or include crystalline components, so an understanding of the physical principles of crystallization from solutions is important.

1.2.1 Nucleation

The process by which a crystalline phase first develops in a saturated solution is termed nucleation. Nucleation happens via the formation of small crystal nuclei in the large volume of the solution. The solution is metastable, which means that the formation of crystals involves passage over a free energy barrier. Nucleation of crystals from solution can occur by two processes: heterogeneous nucleation and homogeneous nucleation. The former happens in the presence of a foreign substrate or surface that reduces the energy barrier. The formation of biominerals mostly begins by heterogeneous nucleation. In homogeneous nucleation, on the other hand, crystal nuclei spontaneously form in the absence of any impurities [14].

When a solution of ions is supersaturated, ionic clusters of a critical size can form spontaneously and homogeneous nucleation occurs. The surface free energy of the solid-liquid interface, $\Delta G_{surface}$, and the energy released by the formation of bonds within the cluster, ΔG_{bulk}, determine the total free energy of nucleation associated with the formation of the cluster. The total change in free energy associated with the formation of the crystal is

$$\Delta G_N = \Delta G_{surface} + \Delta G_{bulk}\,. \tag{1.1}$$

where $\Delta G_{surface}$ and ΔG_{bulk} are given by

$$\Delta G_{surface} = 4\pi r^2 \sigma, \tag{1.2}$$

and

$$\Delta G_{bulk} = \frac{-4\pi r^3 \Delta u}{3V_m}\,. \tag{1.3}$$

In the above equations, r is the radius of the cluster, σ the free energy per unit surface area, Δu the molar energy of crystallization and V_m the molar volume.

Combining Equations (1.1), (1.2) and (1.3) gives

$$\Delta G_N = 4\pi r^2 \sigma - \frac{4\pi r^3 \Delta u}{3V_m}\,. \tag{1.4}$$

The surface free energy scales as r^2 while the drop in bulk free energy scales as r^3. This means that for a small radius cluster, the increase in $\Delta G_{surface}$ is larger than the drop in ΔG_{bulk}, which results in the energy barrier described previously. The relationship between the radius of the cluster and its free energy of nucleation is illustrated in Figure 1.1.

The difference between the free energy per molecule of the bulk and that of the surface is referred to as the interfacial free energy per molecule. The interfacial free energy acts to destabilize the nucleus, when the radius is smaller than a critical size r^*, i.e. when the increase in surface energy associated with increasing the size of the nucleus is larger than the decrease in bulk free energy, the nucleus is unstable. Typically, such a nucleus will dissolve rather than grow. As soon as the nucleus gets large enough, however, the decrease in free energy associated with the formation of the bulk phase becomes high enough that it dominates the increase in the surface free energy, and increasing the size of nucleus decreases the free total energy of the system. At the critical size $r*$, the free energy of the system is decreased whether the nucleus grows or dissolves [14].

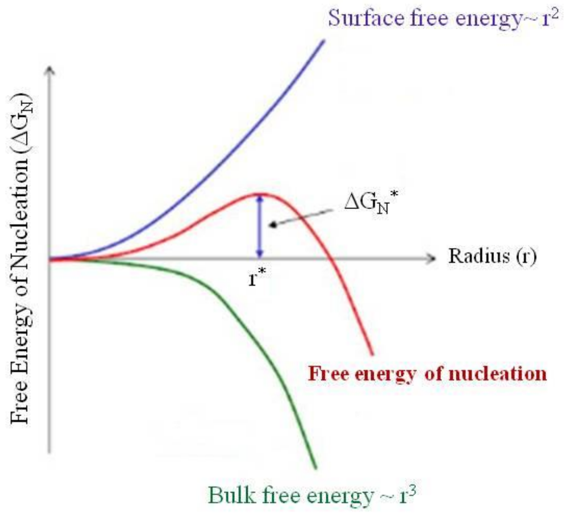

Figure 1. 1: Gibbs Free Energy of Ionic Clusters.

As shown in Figure 1.1, the free energy has a maximum at radius $r*$. This critical radius can be found by taking the derivative of ΔG_N with respect to r and setting it equal to zero. The result is

$$r^* = \frac{2\sigma V_m}{\Delta u}. \tag{1.5}$$

The formation of clusters with radii below the critical radius $r*$ is energetically unfavorable and they will dissolve back into the solution. Increasing the concentration of the solution results in a larger number of collisions among particles and hence the clusters which spontaneously form become larger in size. When the size of a cluster exceeds the critical radius, it will continue to grow, since its free energy decreases for increasing r. The crystal nucleus is now stable.

The maximum value of the free energy of nucleation ΔG_N^* at the critical radius is

$$\Delta G_N^* = \frac{16\pi\sigma^3 {V_m}^2}{3(\Delta u)^2}. \tag{1.6}$$

ΔG_N^* is a measure of the activation energy for nucleation and is related to the rate of nucleation J_N by

$$J_N = Aexp\left(\frac{-\Delta G_N^*}{k_B T}\right). \tag{1.7}$$

Here A is a constant, k_B is the Boltzmann constant and T is the temperature [14,15].

1.2.2 Heterogeneous Matrix-Mediated Nucleation

One type of heterogeneous nucleation is matrix-mediated crystal nucleation. In this process, interactions between the protein matrix and the ions lower the potential barrier for the formation of critical nuclei. The exact process of this mechanism is not yet fully understood [12,16], but one postulated mechanism for matrix-mediated crystal nucleation and growth is illustrated in Figure 1.2. A high-resolution electron microscopy study of the growth of bone minerals showed that the process of crystal nucleation and growth has four stages [17]. In the first step (Figure 1.2 (a)), ions are absorbed on the organic matrix scaffold. The second step (Figure 1.2 (b)) involves the formation of crystal nuclei from the ions, leading to crystal growth (step 3, Figure 1.2 (c)). Step four (Figure 1.2 (d)) is fusion of crystals. This process is extremely sensitive to local variations in structure.

In all biomineralization processes, the chemistry of the organic matrix plays a crucial role in the formation and growth of crystals. This chemistry depends on the amino acid sequence and/or post-translational modifications of proteins in the matrix. Proteins which have been suggested to act as modulators of crystal formation or growth tend to be highly acidic or contain long sequences rich in acidic amino acids and phosphate groups [18]. Some of these proteins, such as bone sialoprotein (BSP), have been found to enhance the process, while others, including osteopontin (OPN), serve as inhibitors of biomineralization [19,20].

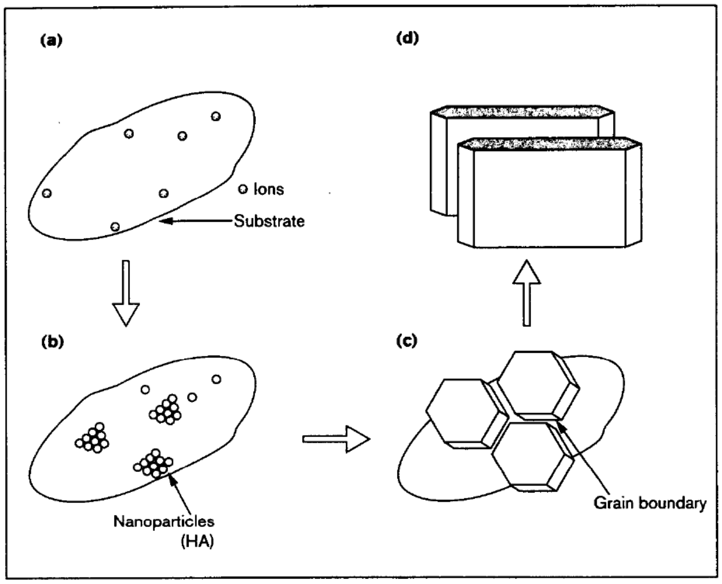

Figure 1. 2: Bone crystal growth mechanism a) ionic adsorption, b) nucleation, c) crystal growth, d) crystal fusion (adapted from [17]).

1.2.3 Growth

After a stable nucleus forms, it will be free to grow. What is necessary for a crystal to grow is that more ions bind to its surface than leave it. Binding tends to take place at specific sites on the surface [14,21]. Steps on the surface of the crystal separate flat terraces at different levels. As illustrated in Figure 1.3, steps at different positions can be connected by kinks. A molecule coming out of the solution makes more bonds to neighboring molecules when it attaches to a kink or at step edges than it does on the flat terraces. Kinks are thus key players in crystal growth. The rate of the crystal growth scales with the kink density, because the probability of the molecules leaving the crystal and returning to the solution from the kinks is much less than from a complete step edge or a site on the terraces. This implies that the growth rate of a crystal can be reduced by preventing incoming molecules from reaching kink sites, or increased by roughening the crystal surface.

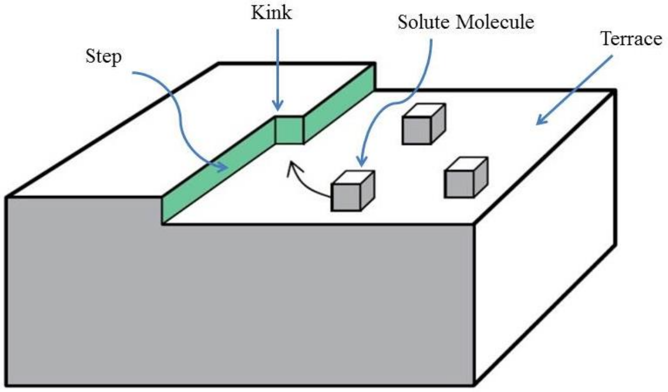

Figure 1. 3: Illustration of a kink and a step on a crystal surface. Solute molecules bind at kinks either directly from solution or after adsorbing and diffusing across terraces.

Organisms are able to control the location and crystallographic orientation of nucleation and the shape of the growing crystallites. The fact that certain organic compounds are found associated with biomineralized structures and their observed effect on crystallization kinetics indicate that these compounds modify the growth stage of minerals in addition to controlling nucleation. In fact, the complex crystal composites and the particular crystallographic orientations that are observed cannot be explained without appealing to some form of active control [14].

One of the most remarkable examples of biomineral growth is bone. It is believed that collagen fibers pack into periodic structures containing rows of small gaps known as "hole zones" 40 nm in length and 5 nm in width, as illustrated schematically in Figure 1.4. When certain proteins interact with this structural framework they induce nucleation of mineral within these gaps, while other proteins regulate the mineral growth process. As the nucleated mineral grows, it expands beyond the hole zones and develops into plates which enclose the collagen [14].

Collagen itself is believed to have no effect on the nucleation of hydroxyapatite. In contrast, some noncollagenous proteins found in the organic part of the bone have been shown to bind to

HA crystals and influence their growth *in vitro* [4]. In particular, extracellular matrix phosphoproteins, which are acidic proteins containing phosphate groups, are known to be involved in triggering and controlling the growth of HA [20, 22].

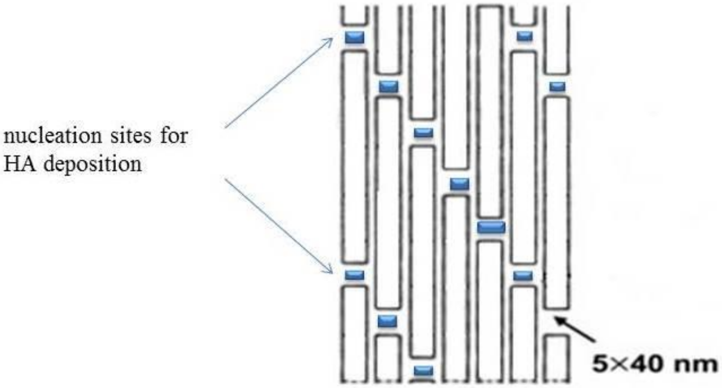

Figure 1. 4: A schematic diagram of collagen matrix undergoing mineralization. The hole zones between collagen molecules act as nucleation sites for HA formation.

The role and action of inhibitory molecules in the biomineralization process is an active area of research. Molecules like osteopontin [23-25] and Matrix Gla Protein (MGP) [26-28] have been demonstrated to inhibit both physiological and pathological HA formation and to affect crystal growth. One possible inhibition mechanism involves the protein binding to an existing crystal surface to inhibit the further deposition of ions. Another involves preventing the formation of critical nuclei by binding to and isolating free calcium. In the latter case the inhibitor decreases the number of nuclei available to grow rather than slowing their subsequent growth [12].

1.3 Proteins

Proteins are large biological molecules consisting of one or more amino acid chains. After synthesis of the primary sequence, many proteins are modified by the addition of various groups including sugars, phosphates, sulphates, and others. This process, termed post-translational modification (PTM), is essential for the functional attributes of many proteins including the proteins that are part of the SIBLING (Small Integrin-Binding LIgand, N-linked Glycoprotein) family of proteins. Phosphorylation is a major PTM within this family. The SIBLINGs are major components of the extracellular matrix of bone and dentin, and have important roles in the mineralization of these tissues. Members of this family include osteopontin (OPN), bone sialoprotein (BSP), dentin matrix protein 1 (DMP1), dentin sialophosphoprotein (DSPP), and matrix extracellular phosphoglycoprotein (MEPE). Phosphorylation of OPN is required for its mineral inhibition capabilities [29,30].

1.3.1 Osteopontin

Osteopontin (OPN) is a highly post-translationally modified phosphoprotein. It has approximately 300 amino acid residues, and its average molecular mass is approximately 44 kDa [31]. Since it has a high content of aspartic acid and glutamic acid residues, including a contiguous aspartic acid sequence, it is strongly negatively charged. The negative charge density is increased by the post-translational modifications [32]. OPN is one of the most abundant non-collagenous proteins, and is present in all body fluids as well as in a range of tissues including bone, kidney, lung and uterus. It is involved in a number of physiological processes in addition to biomineralization, such as cancer metastasis and wound healing [33-35]. Figure 1.5 gives the amino acid sequence of rat OPN [36]. In this figure, each letter refers to an amino acid. The twenty essential amino acids are shown in appendix A.

Data from *in vitro* experiments support the notion that OPN inhibits HA crystal formation, although its structure is similar to BSP [24]. OPN is abundant in highly supersaturated physiological fluids and pathological depositions. For instance, it is the main organic constituent of calcium-oxalate-containing kidney stones [24,32]. OPN is not normally present in blood vessels, but is expressed in atherosclerotic plaque. It has been shown that OPN is expressed by soft tissues to prevent dystrophic calcification [24,37].

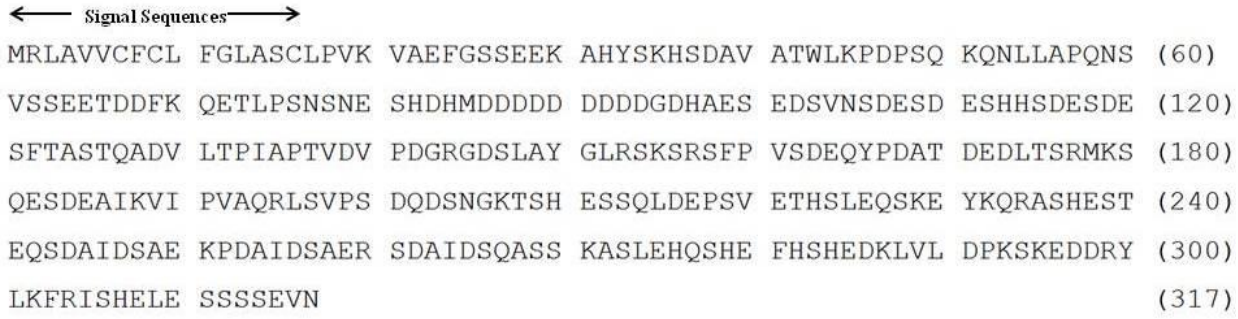

MRLAVVCFCL FGLASCLPVK VAEFGSSEEK AHYSKHSDAV ATWLKPDPSQ KQNLLAPQNS (60)
VSSEETDDFK QETLPSNSNE SHDHMDDDDD DDDDGDHAES EDSVNSDESD ESHHSDESDE (120)
SFTASTQADV LTPIAPTVDV PDGRGDSLAY GLRSKSRSFP VSDEQYPDAT DEDLTSRMKS (180)
QESDEAIKVI PVAQRLSVPS DQDSNGKTSH ESSQLDEPSV ETHSLEQSKE YKQRASHEST (240)
EQSDAIDSAE KPDAIDSAER SDAIDSQASS KASLEHQSHE FHSHEDKLVL DPKSKEDDRY (300)
LKFRISHELE SSSSEVN (317)

Figure 1. 5Amino acid sequence of OPN including the 16 residue signal peptide. Each letter refers to an amino acid and the numbers in the parenthesis are the position of the residue in the complete amino acid sequence [36].

In vitro studies have indicated that native OPN, phosphorylated OPN-derived peptides, and synthetic OPN peptides are strong inhibitors of nucleation [23,24,38,40] and growth [39,40] of HA crystals. Although the mechanism by which mineral formation and growth are inhibited is poorly understood, other studies have shown that OPN also inhibits the formation of other biominerals, such as calcium carbonate [37] and calcium oxalate [41,42]. Hunter and co-workers found that modification of the glutamic acid and aspartic acid residues reduces OPN's inhibitory potency on HA formation [38]. Constant composition studies indicate that aspartic acid is a more effective inhibitor than glutamic acid [38]. It has also been demonstrated that the contiguous aspartic acid segment of OPN participates in preventing HA crystal growth [20,43].

Modulators of crystal nucleation and growth often have altered activities upon immobilization. For instance, OPN is a known inhibitor of HA formation in solution [22,23,38], but when immobilized can induce mineral formation [44]. Phosphorylation plays a key role in OPN's mineral-modulating activity, with phosphorylated OPN or its related peptides being much more inhibitory than the non-phosphorylated recombinant peptides [38,45,46]. It has been reported that the inhibitory potency depends on acidic regions rather than particular chemical groups [24,39].

de Bruyn et al. applied dynamic light scattering to characterize the mechanism of modulation of crystal formation. Their investigation showed that both nOPN and p-rOPN, a phosphorylated version of rOPN, inhibit the nucleation of particles from supersaturated calcium phosphate solution. On the other hand, rOPN, which lacks the phosphorylations of nOPN, acted as an inhibitor of HA growth but not the nucleation [75].

Molecular dynamics simulations have helped elucidate the inhibition mechanism. Grohe et al. [30] found that phosphate groups had a significant role in bringing the peptide close to the crystal surface. They simulated three forms of the same OPN peptide (P0, P1, P3), which have the same amino acid sequence but different numbers of phosphorylations, interacting with a calcium oxalate monohydrate crystal. Another group performed simulations on phosphorylated OPN peptides in the presence of calcium oxalate, and also concluded that phosphate groups are involved in the inhibition of crystal growth [46].

Table 1. 1: Sequences of OPN-derived peptides used in this work.

Peptide Name	Amino acid #	Sequence	Molecular Weight (g/mol)
P0	220-235	SHESTEQSDAIDSAEK	1733.7
P3	220-235	pSHEpSTEQSDAIDpSAEK	1972.64
OPAR (osteopontin poly-aspartate region)	65-80	SHDHMDDDDDDDDDGD	1833.60
pOPAR	65-80	pSHDHMDDDDDDDDDGD	1913.58

Although phosphorylation of OPN seems to be essential to its capability to prevent mineral growth, it is not clear whether phosphorylation at particular sites in the protein is needed. In this thesis, we address this issue by testing some peptides for their effect on HA formation and growth using dynamic light scattering. The peptides listed in Table 1.1 were studied. P0 and P3 corresponded to amino acids 220-235 of the native OPN protein, or residue 236-251 of the OPN sequence that includes the N-terminal signal peptide (Figure 1.5). P0 has no phosphorylations while P3 has three. Similarly, OPAR and pOPAR, while correspond to amino acids 65-80 of the native OPN protein, were studied. OPAR has no phosphorylations while pOPAR has one.

1.3.2 Bone sialoportein

BSP is an acidic phosphoprotein which has been shown to be a nucleator of hydroxyapatite *in vitro* and capable of binding type I collagen [47,48]. Nucleation activity of BSP was first shown by Hunter and Goldberg in 1993 [20] in steady-state double-diffusion experiments using agarose gels. At concentrations of 5.5 mM Ca^{+2} and PO_4^{-3}, no precipitation occurred in the gels unless BSP was included. X-ray diffraction revealed that the recovered precipitates were HA.

```
MVSMKNFHRRIKAEDSEENGVFKYRPRYFLYKHAYFYPPL (40)
            1 →                    ← 1
KRFPVQGGSDSSEENGDGDSSEEEGEEEETSNEEENNEDS (80)

EGNEDQEAEAENATLSGVTASYGVETTADAGKLELAALQL (120)
               2 →                    ←2
PKKAGDAEGKAPKMKESDEEEEEEEEEENENEEAEVDENE (160)

QVVNGTSTNSTEVDGGNGPSGGDNGEEAEEASVTEAGAEG (200)

TTAGVRELTSYGTTAVLLNGFQQTTPPPEAYGTTSPPARK (240)

SSTVEYGEEYEQIGNEYNTAYETYDENNGEPRGDTYRAYE (280)

DEYSYYKGHGYEGYEGQDYYYHQLVPRGSHHHHH       (314)
```

Figure 1. 6: Rat BSP amino acid sequence (adopted from [50]). The amino acid number refers to the position of the residue in the complete amino acid sequence, 1→ ←1 and 2→ ←2 refer to the first and second poly-glutamic acid sequences.

Physiological expression of BSP is essentially restricted to mineralized tissues such as bone, cementum (the calcified substance covering the root of a tooth), dentin and enamel [49]. Mammalian BSPs contain approximately 314 amino acids, including a 16-residue signal sequence [47,50]. Figure 1.6 illustrates the amino acid sequence of rat BSP. The molecular weight of mature BSP extracted from rat bone is 52.5 kDa [51], but there is much variability in this weight as BSP undergoes a number of heterogeneous post-translational modifications. Electron microscopy has shown that BSP has a rod-shaped core with an average length of 40 nm [52]. BSP expression is upregulated at times of first mineral deposition in mineralized tissues.

Its expression is also associated with pathological calcification. BSP expression has been observed in breast cancer [53], prostate cancer [54], lung cancer [55] and thyroid cancer [56], and it has been noted that BSP expression leads to the formation of HA crystals in carcinogenic tumors of the breast and increased metastasis of the cancer cells to bone [53].

As discussed above, BSP is a modulator of mineral formation in steady-state agarose gels [20,22]. Analysis of the effect of BSP on HA formation indicated that this activity is associated with two regions of the protein, each of which consists of a sequence of contiguous poly-glutamic acid residues [50,57]. While one domain is more effective than the other, neither is as potent as the full molecule [58]. BSP also contains several phosphates, which are found mainly on serine residues. A high proportion of Glu residues (approximately 22% of total amino acids) plus sulfate and phosphate groups make BSP highly acidic. The phosphorylations play a role in BSP's ability to nucleate crystal formation, though BSP without PTMs can still promote crystal formation [50].

Fisher in 2001 [59], Wuttke in 2001 [60], and Tye in 2003 [50] showed by NMR (nuclear magnetic resonance), circular dichroism and small angle x-ray scattering respectively that BSP has a loose, flexible structure. In contrast, many other proteins have a stable three-dimensional structure. The unstructured nature of BSP likely allows BSP to interact with multiple partners including HA [48], collagen [61], matrix metalloproteins-2 [62] and Factor H [63]. BSP also contains an integrin-recognition sequence Arg-Gly-Asp (RGD) located near the carboxy-terminal end of the molecule [57]. The RGD sequence promotes cell attachment, mediates cell signaling and has been shown to promote osteoprogenitor cell differentiation into osteoblasts [20,64].

Molecular dynamics (MD) is a powerful computer-based technique for predicting the interactions between small molecules at the atomic scale. Since crystals have a repeating 3D lattice, the interaction between peptides and crystal faces can be studied using MD simulations. Baht et al. performed MD simulations to investigate the nucleation mechanism of BSP [65]. Bone sialoprotein has two glutamic-acid-rich domains located at residues 42–100 and 133–205. Baht et al. simulated the regions BSP-(59–74) and BSP-(133–148) interacting with the {100} crystal face of HA. They found that for phosphorylated BSP-(133–148) every other glutamic acid is able to interact with the surface of the hydroxyapatite crystal to form an electrostatic bond. This binding was less pronounced for non-phosphorylated BSP-(133–148). The phosphorylated peptide contained a longer, more-extended alternating pattern of bonds. This difference may explain why nucleation activity is enhanced in the phosphorylated form of the peptide [65]. Previous work by Tye et al. has shown that rBSP-(42-100), which also contains a Glu-rich region, does not nucleate HA [50]. Simulations of rBSP-(59-74) revealed that, despite having sites of phosphorylation, this peptide presented quite a different spatial distribution of side chains and did not adopt the pronounced alternating structure [65]. This suggests that a particular sequence of amino acids, in this case poly-Glu, is not the only factor that determines the nucleation potency of the peptide, and that the peptide structure is also important. On the other hand, Yang et al. also explored the possible role of BSP in nucleation of HA by molecular dynamic simulations [66]. Their results indicated that the sequence of poly-Glu residues plays a key role in the nucleation of amorphous calcium phosphate clusters which develop into crystalline hydroxyapatite.

Mice lacking BSP are viable and breed normally, but there is a significant bone phenotype in young animals. It has been noted that there is a decrease in mineralization of cortical bones (the outer shell of the bone which is dense and contributes about 80% of the human skeleton) and shortened long bones for 0-4 months mice lacking BSP; however, this is overcome by the time the animals are 12 months old [67].

In 1996 Hunter et al. reported that in solution studies, BSP at concentration up to 10 μg/ml had no effect on hydroxyapatite formation [22]. An inhibitory effect of BSP and its peptides on crystal growth in a system of seeded HA crystals was observed by Stubbs et al. [68].

1.4 Methods for Characterization of Protein Modulation of Mineralization

1.4.1 Steady State

The effectiveness of crystal nucleator and inhibitor proteins is generally assessed using the steady state method. This makes use of a number of plastic cells containing agarose gels which are arranged in parallel. Calcium and phosphate solutions are separately pumped into the cells, as illustrated in Figure 1.7. Spent solutions are collected in a reservoir connected to the outlet of the cell. A dialysis membrane separates both solution paths from the agarose gel in the center of the cell. Ions can diffuse across the membrane into the gel, forming a concentration gradient in the gel. Protein is premixed with the agarose in solution so it is evenly distributed and the agarose is then allowed to gel. The effect of the protein on nucleation can be assessed by observing the protein concentrations at which nucleation of hydroxyapatite takes place. Control experiments are conducted with no protein present. At the end of the experiment, the gels are examined to determine the calcium and phosphate content [20]. Although this technique has been used to determine the nucleation potency of a number of proteins including BSP, BSP-derived peptides, and other bone-related proteins, it has two major disadvantages. The method is very time-consuming and requires at least five days to run a single experiment. In addition, it cannot be used to study the kinetics of the nucleation and growth process, but can only reveal whether or not mineralization has occurred.

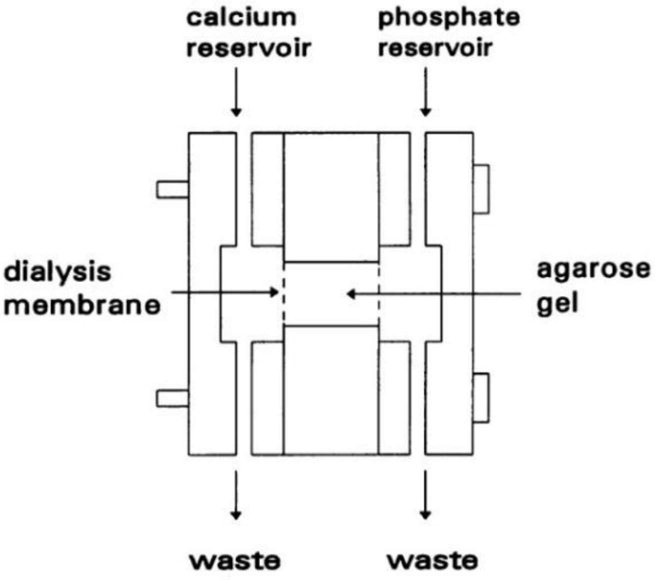

Figure 1. 7: Steady-state agarose gel system [adapted from 20].

1.4.2 Constant Composition Method

Another commonly used method of assessing the modulating potency of proteins and peptides is the constant composition method, which examines the effect of proteins on the growth of pre-seeded HA crystals placed in a solution of calcium and phosphate ions [39]. Figure 1.8 illustrates this method. Seed crystals are added to a continually mixed, metastable solution of calcium and phosphate ions at *p*H 7.40. As the crystal grows, OH^- ions are used up, reducing the *p*H of the solution. This causes more calcium, phosphate, and sodium hydroxide to be released into the solution by an autotitrator to maintain the *p*H at the desired value. This feedback loop ensures that the composition of the calcium phosphate solution remains unchanged over the course of the experiment. Dissolution of carbon dioxide in the solution is prevented by bubbling nitrogen gas through it. The total amount of calcium released by the autotitration system yields a measurement of the crystal growth and can thus be used to generate titration curves.

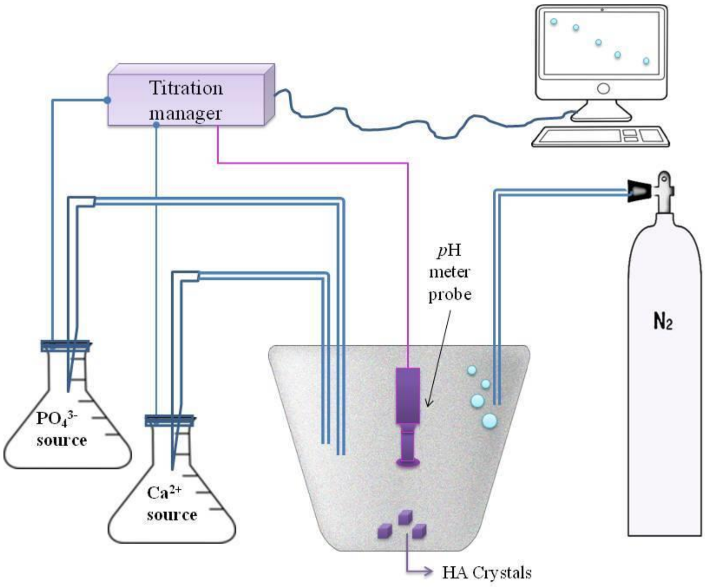

Figure 1. 8: Constant composition system.

When inhibitor proteins are added to the calcium phosphate solution, the consequent decrease in the growth rate of the crystal is revealed through a lower volume of titrant added to the solution.

Comparison of the growth rate in the presence of the inhibitor at different concentrations with the results of the control experiment yields the protein's inhibition potency. The constant composition method is an accurate technique for the measurement of the effect of inhibitors on crystal growth and has been used to characterize proteins such as OPN [39]. This method is technically difficult and time consuming and, since it uses seed crystals, it gives no information on the effects of the protein on nucleation.

1.4.3 Dynamic Light Scattering

Light scattering is defined as the deflection of an incident beam of light by small particles. Lord Rayleigh pioneered the use of light scattering as a technique to study colloidal systems. When radiation with a given wave vector is incident on a medium, some of it will be scattered by the medium. A detector positioned at an angle θ relative to the incident radiation will measure the intensity of the scattered radiation, $I(\theta,t)$. The scattering medium in our experiments is a suspension of small particles of precipitating calcium phosphate which over time will become HA. Since the scattering particles diffuse through the medium, $I(\theta,t)$ fluctuates over time.

The scattering vector $\boldsymbol{q}$ is the difference between the propagation vectors of the scattered and incident beams. The magnitude of the scattering vector q is given by

$$q = \frac{4\pi n_0}{\lambda_0}\, sin\left(\frac{\theta}{2}\right), \tag{1.8}$$

where n_0 is the refractive index of the scattering medium and λ_0 is the wavelength of the light in vacuum.

The angular distribution of the intensity of light scattered from a colloidal suspension depends on the size of the suspended particles, the optical properties of the scatterers (such as their polarizability and refractive index) and the wavelength of the incident light. In a basic light scattering setup, one measures the average scattered intensity I_s or the energy spectrum of the time dependent intensity, $S(\omega)$. I_s contains information about the static properties of the scatterers

while $S(\omega)$ depends on their dynamics. Depending on which of these quantities is measured, therefore, light scattering experiments are generally classified as either static light scattering (SLS) or dynamic light scattering (DLS). In SLS, the average scattering intensity is measured as a function of scattering angle. Static light scattering measurements provide structural information about the scatterers such as molecular weight, radius of gyration, and shape as well as information about their spatial ordering [69].
One useful and versatile technique to monitor the effect of proteins on the formation and growth of hydroxyapatite is DLS. In dynamic light scattering, one measures the time dependence of the scattered intensity. DLS can be used to acquire information about the effective hydrodynamic size of the suspended scatterers. Most previous studies of hydroxyapatite crystals growth have been carried out using constant composition seeded growth, but in 1998 Onuma et al. observed calcium-phosphate clusters with sizes around 1.0 nm in simulated body fluid using an intensity-enhanced dynamic light scattering technique. Their report showed the stability of clusters over time. Their suggested model for cluster growth was that small calcium phosphate clusters packed together to form HA crystals [70].

The stable nanometer-sized calcium-phosphate clusters were detected in a solution containing these ions by DLS by Oyane and co-workers in 1999. They investigated the effect of concentration and *p*H of the solution on size distribution. They also showed that the concentration of clusters decreased when the supersaturation of the solution with respect to HA was decreased [71]. Omuna et al. also studied the precipitation kinetics of HA using a continuous-angle laser light scattering technique, and measured the molecular growth units of HA crystals [72].

Fibroblast growth factor-2 (FGF-2), is important in human hard tissue formation and has been studied by several groups. Onuma et al. adopted dynamic light scattering to monitor the size distribution of FGF-2 in solutions and the process of converting amorphous calcium phosphate to hydroxyapatite [73]. Kamiya et al. also used DLS to study the effect of lanthanum doping on the size distribution and growth of calcium carbonate crystals precipitating from solution. They found that the presence of La^{3+} ions caused the particles to grow slowly [74].

More recently de Bruyn et al. applied dynamic light scattering to characterize the mechanism of modulation of crystal formation. To evaluate the effect of PTMs, three isoforms of OPN –

nOPN, rOPN and p-rOPN – were examined. Their investigation showed that both nOPN and a phosphorylated version of rOPN, p-rOPN, inhibit the nucleation of particles from supersaturated calcium phosphate solution. On the other hand, rOPN, which lacks the phosphorylations of nOPN, acted as an inhibitor of HA growth but not the nucleation [75].

The effect of matrix gla protein (MGP) peptides on the *in vitro* formation of HA was also investigated by DLS by Goiko et al. [27]. MGP is a phosphorylated and γ-carboxylated protein which prevents the deposition of HA in the walls of blood vessels and kidney. To distinguish the effect of phosphorylation and γ-carboxylation on HA nucleation, MGP-derived peptides containing these modifications were compared to unmodified peptides. Their results indicated that the inhibitory effects on nucleation were dependent on these modifications, and that γ-carboxylated groups, similar to phosphorylation, enhances inhibitory activity [27].

1.5 Purpose of this Thesis

The details of the process of biomineralization are complex and not completely understood. It is known that certain proteins play key roles in both the initial nucleation of biomineral crystals, and in the regulation of their growth. Some have been observed to enhance nucleation and/or growth while others act as inhibitors. Controlled biomineralization is vital for mammalian life, and unregulated mineralization can lead to pathological deposition, causing serious medical diseases. There is, therefore, considerable motivation for characterizing and understanding the process of biomineralization, and in particular the role of protein on nucleation and growth regulation.

This project began with the goal of studying the effect of BSP on both nucleation and inhibition. Previous work by Hunter et al. in 1993 [20] and Baht et al. in 2008 [47] demonstrated BSP-mediated nucleation of HA using agarose and collagen gel-based systems, respectively. Dynamic light scattering provides an alternative method of investigating the kinetics of nucleation and growth of hydroxyapatite crystals in the presence of bone-related proteins or synthetic peptides. Based on our group's success at studying inhibition of mineral formation using dynamic light scattering [27,75], we initiated DLS studies to characterize early nucleation events mediated by

BSP. Such results would have provided valuable insight into the nucleation process in biomineralization. However, we had difficulty in finding the correct conditions to study nucleation, so this study evolved to focus on inhibition of mineral formation.

The present work uses dynamic light scattering to characterize the inhibitory effects of BSP, OPN, and OPN-derived peptides on hydroxyapatite formation and growth. To examine the effects of phosphate groups, both phosphorylated (P3 and pOPAR) and non-phosphorylated (P0 and OPAR) peptides were studied. The goal of this study is to help elucidate the process of biomineralization. Ultimately, understanding of this process could lead to the development of peptide therapies to control pathological calcifications that result from the breakdown of the body's natural biomineralization regulatory system.

Chapter 2: Methods

2.1 Dynamic Light Scattering

2.1.1 Theory of Dynamic Light Scattering

In dynamic light scattering, laser light is scattered by a collection of suspended particles, and the intensity of scattered light is measured at a particular angle with a photomultiplier detector (Figure 2.3). In a colloidal suspension, the motion of the particles is random and is due to Brownian motion. The total scattered electric field at the detector is the superposition of the scattered fields due to all of the particles. In the scattering volume, which is the volume that is both illuminated by the incident beam and observed by the detector [76], the positions of the particles vary in time, so the phase of each scattered wave arriving at the detector fluctuates in time, and *E(t)*, the total scattered electric field at the detector, also fluctuates. This in turn causes fluctuations in the intensity, which is defined as

$$I(t) = |E(t)|^2, \tag{2.1}$$

where *t* is the time. These fluctuations in the scattered intensity are the key concept of DLS experiments. DLS involves measuring the fluctuations in the intensity of the scattered light and analyzing them to the extract information. The time scale of these fluctuations depends on the size of the diffusing particles [76], so they can be analysed to calculate the average size of a particle diffusing in solution. Small particles diffuse more quickly, and so cause a rapidly fluctuating signal, whereas larger particles diffuse more slowly, resulting in more slowly varying fluctuations. Figure 2.1 shows a schematic example of an intensity-time plot for small and large particles.

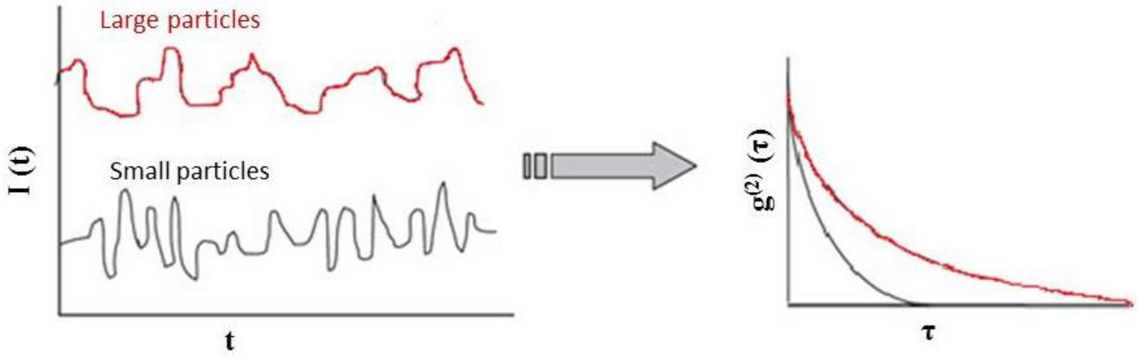

Figure 2. 1: Left: A schematic illustration of the fluctuations in scattered intensity observed for scattering from large and small size particles, Right: Correlation functions for large and small size particles.

It should be emphasized that the fluctuations in the scattered intensity do not result from changes in the number of particles in the scattering volume, but from changes in the position of the scatterers. We can get quantitative information out of these fluctuations by examining the decay of their autocorrelation function. The intensity autocorrelation function $C(\tau)$ shows the correlation between scattered intensity at a given time t and a later time $t+\tau$. In order to get good statistics, this comparison is normally made at many different values of t and averaged. If one denotes the scattered intensity at an arbitrary time by $I(t)$ and that at a later time τ by $I(t+\tau)$, the autocorrelation function is

$$C(\tau) = \langle I(t)I(t+\tau)\rangle. \tag{2.2}$$

Here, the angle bracket represents an average over time. When τ=0 the two signals are the same since the particles have not moved from their initial position and the correlation is high. If the sampling time interval τ is very large, there is no correlation between the pairs of sample intensities and the above equation becomes

$$C(\infty) = \langle I(t)I(\infty)\rangle = \langle I(t)\rangle^2. \tag{2.3}$$

In our experiment, a digital correlator takes the digitized photo-count measured by the detector, which is proportional to $I(t)$, and then computes the correlation function. This function then is normalized by the value of the correlation function at long times, $C(\infty)$. The normalized correlation function of the scattered intensity is referred to as $g^{(2)}(\tau)$ and is given by

$$g^{(2)}(\tau) = \frac{\langle I(t)I(t+\tau)\rangle}{\langle I(t)\rangle^2}. \tag{2.4}$$

If the scattering is a Gaussian process, $g^{(2)}(\tau)$ is related to the autocorrelation function of the electric field, $g^{(1)}(\tau)$, by the Siegert relation [77]

$$g^{(2)}(\tau) = 1 + \beta\left(g^{(1)}(\tau)\right)^2, \tag{2.5}$$

where β is a constant that depends on the size of the detector and the details of the optics of the experimental set up. If the particles are spherical, monodisperse, and undergo Brownian motion, the autocorrelation function of electric field, $g^{(1)}(\tau)$, decays exponentially with delay time:

$$g^{(1)}(\tau) = \exp(-Dq^2\tau), \tag{2.6}$$

where D is the translational diffusion coefficient. One can find the hydrodynamic radius, which is the quantity of interest in the present work, from D using the Stokes-Einstein relation,

$$r_h = \frac{k_B T}{6\pi\eta D}. \tag{2.7}$$

Here $k_B$is the Boltzmann constant, T is the absolute temperature, and η is the viscosity of the solution. If the scattering particles are not spherical, DLS measurements provide the apparent hydrodynamic radius of the particles being examined. If they are polydisperse, $g^{(1)}(\tau)$ can be expressed as an integral over a distribution of decay rates, from which the distribution of sizes can in principle be determined [69,77].

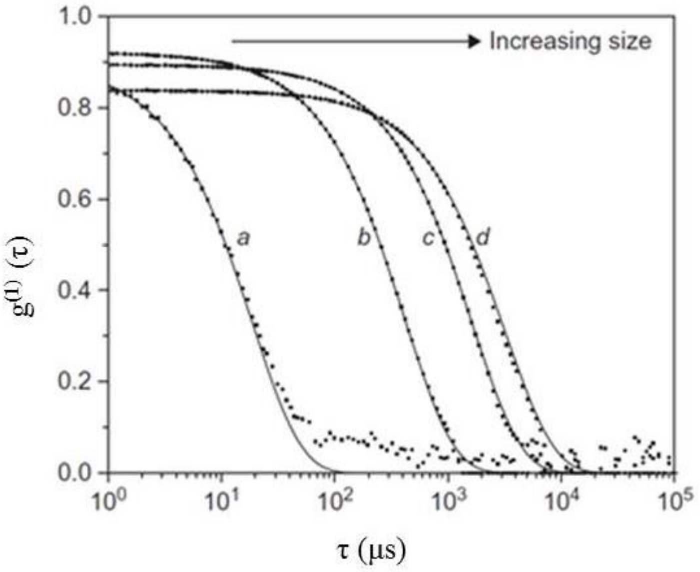

Figure 2. 2: A typical example of autocorrelation function for different-sized particles. The curves are fit to an exponential decay. The fitted values for the radii are a=2.5 nm, b=54 nm, c=214 nm and d=422 nm. [69].

Figure 2.2 depicts the dependence of the electric field correlation function, $g^{(1)}(\tau)$, on time interval τ for nanoparticle scatterers with different sizes. A line has been fitted to data by assuming a single exponential decay. From the figure we can infer that as the size of the particles becomes larger, the decay of the correlation function shifts to a longer time. The average hydrodynamic size of particles can be roughly evaluated by using this shift.

In this thesis, the sample studied is a suspension of small calcium phosphate crystals precipitating from solution. Measurement of the intensity autocorrelation function as a function of time allows us to follow the changing hydrodynamic radius of the crystals as they grow.

Moreover, the average scattered light intensity can be computed as a function of time, allowing for at least a qualitative measure of the concentration of scatterers. As a result, DLS not only allows us to assess the effect of the proteins on the growth rate but also on the nucleation of hydroxyapatite crystals.

2.1.2 Dynamic Light Scattering Experiment

The effects of proteins on the nucleation and growth of crystals can be studied using dynamic light scattering (DLS). This technique is very effective for measuring the sizes of small particles as well as for studying protein-protein interactions. It has also been extensively used to examine the conditions that affect protein crystallization through assessing the sample homogeneity [70,78,79]. DLS has been used to study the full native and recombinant OPN protein [75], but it has not been used to study BSP.

Our DLS experimental set-up is schematically depicted in Figure 2.3. The light source is a HeNe laser with a wavelength of 632.8 nm and power of 22 mW. A CGS-3 compact goniometer system manufactured by ALV-GmbH was used to perform the scattering measurements. A photomultiplier detector is positioned on one arm of the goniometer, and can be rotated to measure the scattered light intensity at angles ranging between 12° and 155°. The photomultiplier signal is passed to an amplifier, and the digitized output is received by a digital correlator which calculates the intensity autocorrelation function, $g^{(2)}(\tau)$, in real time. The intensity autocorrelation function is then sent to a computer along with the intensity-time data. A MATLAB program written by Dr. de Bruyn, which will be discussed below, performs curve fitting on the autocorrelation function to determine the distribution of hydrodynamic radii of the scatterers.

The experiments described in this thesis were all performed at a scattering angle of 90°. The samples were placed in a clean cylindrical cuvette with a radius of 5 mm and made of optical quality glass. The cuvette is positioned in a chamber at the center of a circular vat filled with toluene. Since the refractive index of toluene is close to that of the glass, this minimizes stray scattering from the surface of the cuvette. The temperature of the toluene bath was kept constant at 25°C by a temperature controlled circulating bath. The measurements for a given concentration of protein or peptide were carried out over a 40 minute period. The intensity autocorrelation functions and mean scattered intensity were calculated from the accumulated data every 30 seconds.

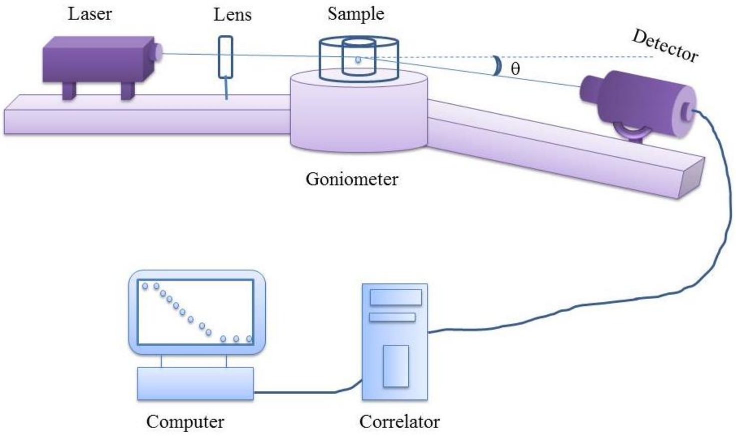

Figure 2. 3: The experimental set up of the light scattering instrument.

2.1.3 Data Analysis

Because of the random motion of the scattering particles, the autocorrelation function of scattered electric field, $g^{(1)}(\tau)$, will decay as τ increases. The hydrodynamic radius of the scatterers, which is the radius of a sphere that would have the same average diffusion constant as the scattering particles, is calculated from its decay rate. For a system of monodisperse scatterers, $g^{(1)}(\tau)$ decays exponentially with delay time. In our experiment, we have polydisperse scatterers, so $g^{(1)}(\tau)$ will not have a simple exponential decay. As discussed in [70,77] the first two terms of a cumulant expansion for $g^{(1)}(\tau)$ are

$$g^{(1)}(\tau) = \exp(-\bar{\Gamma}\tau)\left(1 + \frac{\mu_2}{2}\tau^2\right). \tag{2.8}$$

where $\bar{\Gamma}$ is the mean relaxation rate of $g^{(1)}(\tau) - 1$, and μ_2 is its second moment. The electric field autocorrelation function $g^{(2)}(\tau)$ is related to $g^{(1)}(\tau)$ by Equation (2.5), which, using Equation (2.8) can be written as

$$g^{(2)}(\tau) = B + \beta \exp(-2\bar{\Gamma}\tau)\left(1 + \frac{\mu_2}{2}\tau^2\right), \tag{2.9}$$

Here the baseline, *B,* is approximately one, but varies due to noise. We determined $\bar{\Gamma}$ and μ_2 from the measured intensity autocorrelation function using a standard non-linear least-squares fitting routine. Once $\bar{\Gamma}$ and μ_2 were computed from the fits, the mean hydrodynamic radius, $\bar{r}_h$, was calculated using Equations (2.6) and (2.7) as

$$\bar{r}_h = \frac{k_B T q^2}{6\pi\eta\bar{\Gamma}}. \tag{2.10}$$

We used $n = 1.33$ and $\eta = 8.90 \times 10^{-4}\ Pa\ s$, for the refractive index and viscosity of water at 25°C.

The standard deviation of the Gaussian size distribution is

$$\sigma_r = \sqrt{\mu_2}\,\frac{\bar{r}_h}{\bar{\Gamma}}. \tag{2.11}$$

2.2 Identification of Precipitates

The crystals precipitated in our experiments were extracted from the solutions and identified by X-ray diffraction. Details of this technique and the method for harvesting the crystals are described in this section.

2.2.1 X-ray crystallography

X-ray crystallography is a powerful and non-destructive technique for determining the crystal structure of many kinds of materials, including solid crystals, powders, and biological macromolecules such as proteins.

X-rays are electromagnetic radiation with energies above ultraviolet light and below gamma rays. The wavelengths of X-rays are in the range 0.1-100 Å and their energy is between 120 keV and 0.12 keV.

2.2.2 X-ray diffraction from a crystal: Bragg's Law

A crystal is composed of periodic planes of atoms. The planes are indexed by a set of integers indicating their direction. Atoms in each plane scatter incident X-rays. If every atom scatters X-rays as shown in Figure 2.4, then constructive interference will be observed at certain angles. The light waves constructively interfere when they are exactly in phase. Assuming that the incident waves 1 and 2 in Figure 2.4 are in phase when emitted from their source, then the condition for them to interfere constructively after scattering is that the additional distance *2x* traveled by wave 2 is equal to an integer number of wavelengths. Since

$$x = dsin\theta, \tag{2.12}$$

where d is the distance between the planes and θ is the angle between the incident X-ray and the plane, a diffraction peak is observed when

$$n\lambda = 2dsin\theta. \tag{2.13}$$

This equation is known as Bragg's Law. As seen in Figure 2.4, the angle between the incident and diffracted beams is 2θ. Bragg's law is derived assuming that the atoms are exactly above each other on the planes, but in fact, they can be located anywhere on the planes [80,81,90].

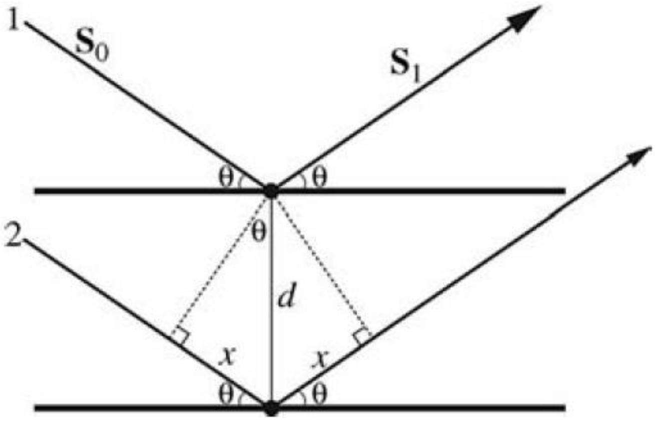

Figure 2. 4: X-rays scattering from two parallel planes. S0 indicates the incident X-ray beam and S1 the diffracted beam [81].

2.2.3 Crystal Preparation

The amount of precipitate formed in one 1.8 ml sample tube is very small. Roughly 1 mg of the precipitate is needed for X-ray diffraction analysis, so several reaction mixtures in tubes were prepared in parallel to obtain sufficient material for analysis.

The precipitation was allowed to take place for 40 minutes, the same length of time as the DLS experiments. The solutions from all of the test tubes were then transferred to microfuge tubes and centrifuged at 8000g for 2 minutes. The supernatant liquid was removed using a pipette, and the crystals were washed with 100 µl or more *p*H10 water. *p*H10 water is a mixture of 10% ammonium hydroxide and deionized water and is used to stop the reaction between calcium and phosphate ions. The tubes were shaken gently to wash the crystals well and centrifuged again for 2 minutes. The *p*H10 water was then removed and 100 µl or more 100% ethanol was added to the tubes. Once again, the microfuge tubes were gently tapped, and then all the contents were combined into a single tube and centrifuged for 2 minutes. The ethanol was removed and the collected precipitant dried at room temperature and stored in a dessicator.

The precipitate was analyzed with a Bruker D8 Discover micro X-ray diffractometer using Cobalt Kα radiation (1.78897 Å) (performed by Prof. Roberta Flemming and Michael Bramble from Western's Department of Earth Sciences). The crystal structure was identified by comparing the measured diffraction pattern with catalogued standard patterns from the International Centre for Diffraction Data (ICDD) database.

Chapter 3: Materials

3.1 Preparation of Solutions

A significant amount of time was spent to find the appropriate concentrations of reagents and preparation technique that resulted in reproducible results.

For our studies of nucleation and inhibition, four 100 ml stock solutions of sodium chloride (NaCl), sodium phosphate dibasic (Na_2HPO_4), tris (hydroxymethyle) aminomethane ($C_4H_{11}NO_3$), and calcium chloride ($CaCl_2$) with concentrations of 2.0M, 0.25M, 1.0M, and 0.5M respectively, were prepared using deionized water. All of the chemicals were purchased form Sigma-Aldrich Inc and had purities of above 99%. To remove bacteria and minute particles, the solutions were filtered through 0.2 μm membrane filters (Nalgene). The stock solutions were kept in clean, autoclaved bottles. Stock solutions were normally made fresh every two weeks to ensure reproducible results.

Three 50 ml working solutions were prepared daily from the stock solutions. The working solutions were: a calcium solution consisting of 12 mM $CaCl_2$, 150 mM NaCl, 18.75 mM Tris; a phosphate solution containing 7.5 mM Na_2HPO_4, 150 mM NaCl, 18.75 Tris; and a Tris solution with 150 mM NaCl and 18.75 mM Tris. The *p*H for each solution was adjusted to 7.40 by adding dilute NaOH or HCl. This *p*H and the NaCl concentration were chosen to mimic *in vivo* conditions. Since any contaminants could scatter light and skew the results, the solutions were filtered a second time through fine 0.02 μm Whatman syringe filters directly into sterile BD falcon tubes. These final working solutions were only used on the day of preparation to ensure reproducible results.

In order to find suitable control conditions for hydroxyapatite crystal formation and growth, we prepared and tested solutions with different concentrations of calcium and phosphate ions. The rate of crystal growth should be slow enough to allow time to perform a measurement, but fast enough that a significant change in the crystal size took place over the forty-minute duration of the experiment. The growth rate is very sensitive to small changes in *p*H and temperature, so we had to slightly change the concentration of Ca^{2+} and PO_4^{3-} for experiments performed on different days. Each day, the selected control concentrations of ions were then used for all experiments on that day.

Tables 3.1 and 3.2 give the Ca^{2+} and PO_4^{3-} concentrations and volumes that were used in each protein or peptide-containing run. All concentrations of a given protein or peptide were tested on the same day. For each run, the ratio of Ca^{2+} and PO_4^{3-} was maintained at 1.60, which is the most favorable value for hydroxyapatite formation.

Table 3. 1: The concentration and volume of Ca^{2+} and PO_4^{3-} solutions used for protein runs.

Protein	$[Ca^{2+}]$ (mM)	V_{Ca} (µl)	$[PO_4^{3-}]$ (mM)	V_{PO4} (µl)
nOPN	5.800	870	3.625	870
rOPN	5.400	810	3.375	810
rBSP	5.200	780	3.250	780
rBSP	5.400	810	3.375	810

Table 3. 2: The concentration and volume of Ca^{2+} and PO_4^{3-} solutions used for peptide runs.

Peptides	$[Ca^{2+}]$ (mM)	V_{Ca} (µl)	$[PO_4^{3-}]$ (mM)	V_{PO4} (µl)
P0	5.460	820	3.416	820
P3	5.400	810	3.375	810
OPAR	5.660	850	3.541	850
pOPAR	5.730	860	3.583	860

In all cases, a total volume of 1.8 ml was used. The volumes of calcium and phosphate solutions given in the Tables were combined with sufficient Tris solution to give the required total volume. When an aliquot of dissolved peptide in Tris buffer was added to the solution the volume of Tris solution was reduced accordingly. The required volume of calcium solution, Tris buffer and the protein or peptide under study were combined in a 5 ml borosilicate glass tube, and then the phosphate solution was added to initiate the nucleation of HA. The glass tube was gently inverted three times to mix the solutions, and was then cleaned and immediately put in the sample chamber of the light scattering instrument.

3.2 Proteins and Peptides Preparation

To investigate the role of phosphorylation in biomineralization process, native and recombinant proteins and synthetic peptides containing 0, 1 and 3 phosphate groups were used. The proteins studied were native osteopontin (nOPN), recombinant osteopontin (rOPN) and recombinant bone sialoprotein (rBSP). These proteins were prepared in-house. For example, nOPN was extracted from rat bone and then purified by H. Chen using the protocol described in [82]. Rat nOPN was shown to have a mass of 37600 g/mol, and contained approximately 10 phosphate residues per molecule. Furthermore it is glycosylated and sulfated [75]. Recombinant rat osteopontin, containing a short His-tag for purification purposes, was expressed by BL-21 bacteria and purified [32]. It has a mass of 36046 g/mol and contains the same polypeptide chain as nOPN but without the post-translational modifications. Similarly, rBSP was expressed and purified by H. Chen as described in [50]. One of the serine amino acid of the rBSP used in these studies was substituted by alanine. The rBSP has a molar mass of 34780 g/mol [12].

We also studied the peptides P0 and P3, which correspond to amino acids 220-235 (SHESTEQSDAIDSAEK) of rat OPN and contain zero and three phosphates, respectively, and OPAR and pOPAR, which include amino acids 65-80 (SHDHMDDDDDDDDDGD) of rat bone OPN, and which contain zero and one phosphate, respectively.

Phosphorylated and non-phosphorylated peptides were synthesized by a batch method and purified by Y. Liao as described in [29,30,39]. The final peptide preparations were >98% pure. The peptide masses were obtained using mass spectrometry and are presented in Table 1.1.

All the proteins and peptides were stored at -20°C as pre-weighed freeze-dried aliquots. For the experiments one or more tubes of protein were dissolved into a volume of filtered 0.05 M Tris buffer solution at *p*H 7.4 to achieve a concentration of 1 μg/μl. The amount of protein solution used in individual experiments is indicated in the Results. To prevent degradation of the dissolved protein aliquots they were kept on ice until used.

Chapter 4: Results

4.1 Dynamic Light Scattering Results for Control Experiments

Prior to doing each set of experiments we carried out control experiments with no protein or peptide added to the calcium phosphate solution. The control experiments provide a baseline for the nucleation and growth of hydroxyapatite crystals in the absence of protein or peptide. They also help us to confirm the consistency of the results. Control solutions were prepared using the method described in section 3.1 and Table 3.1 and Table 3.2. The intensity autocorrelation function for one of the control experiments is plotted in Figure 4.1. The red line is a fit to Equation (2.9).

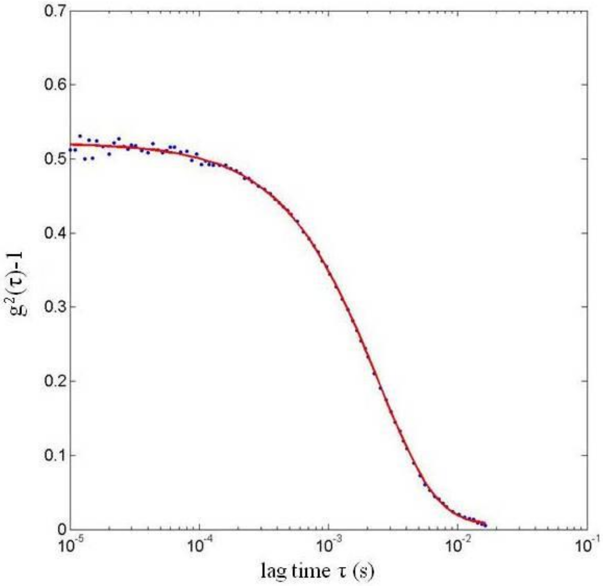

Figure 4. 1: Intensity autocorrelation function for a typical control experiment. The fit to Equation (2.9) is shown as a red curve.

Having determined $\bar{\Gamma}$ from the fit, we can find the mean hydrodynamic radius from Equation (2.10) as described above.

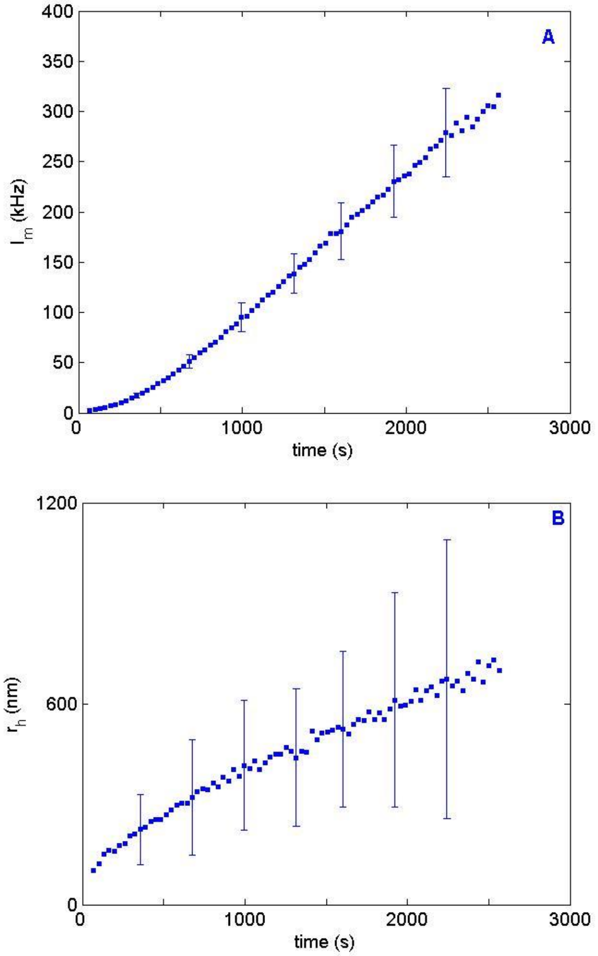

Figure 4. 2: A) The mean scattered light intensity, I_m, and B) the mean hydrodynamic radius of the particles, $\bar{r}_h$ in the absence of protein.

Figure 4.2 (A) shows the time dependence of the averaged scattered light intensity, I_m, as well as the standard deviation of the fluctuating intensity for a typical control experiment. Note the mean value, I_m, is much smaller than these error bars. The averaged scattered light intensity is given in terms of the photon count rate detected by the photo multiplier. During the first two minutes of the experiment, the data are not reliable because of fluid motion due to mixing and placing of the sample in the chamber. Over the duration of the measurements, the scattered intensity increases steadily and relatively linearly as the calcium phosphate precipitates. The scattered light intensity depends in a complex way on the size of the scatterers as well as their concentration [75,76].

For the range of particle sizes relevant here, $I(t)$ is approximately proportional to particle concentration and to $\overline{r_h}^3$ [76,83]. Therefore, the size of the scatterers has more impact on $I(t)$ than their concentration.

The dependence of $\overline{r_h}$ on time for the same control run is shown in Figure 4.2 (B). In this Figure, the error bars, σ_r, represent the standard deviation of the Gaussian distribution of particle sizes obtained from the fit, as described in Equation (2.11). As above, the uncertainty on $\overline{r_h}$ is much smaller than these error bars. At the beginning of the experiment $\overline{r_h}$ is about 120 nm, and it grows to approximately 700 nm at forty minutes. The width of the size distribution is relatively broad and becomes larger as time passes. The growth rate of the precipitating particles is given by the slope of the plot of $\overline{r_h}$ versus time, and is higher at the beginning of the experiment than at the end.

4.2 X-ray Diffraction Result for Control Experiments

The protocol described in section 2.2.3 was used to recover crystals from a control experiment. The results of the X-ray diffraction analysis are shown in Figure 4.3. The diffraction pattern of the precipitate that formed in the control experiment matched well with the ICDD card # 01-073-0293 for hydroxyapatite. The intensity of the Debye rings (results not shown here) is uniform, implying that the crystals are fine grained. The narrow diffraction lines, illustrated in Figure 4.3, demonstrate that the crystals are well-formed. From the width of the peaks the size of the crystals is estimated to be 200 nm. This is slightly less than the value of $\overline{r_h}$ measured with DLS. The red and green lines shown in the figure are expected diffraction peaks for hydroxyapatite and calcium phosphate hydrate respectively. The measured diffraction pattern is very similar to both, but calcium phosphate hydrate is not expected to form under the conditions in our experiments. Our crystals were therefore identified as hydroxyapatite.

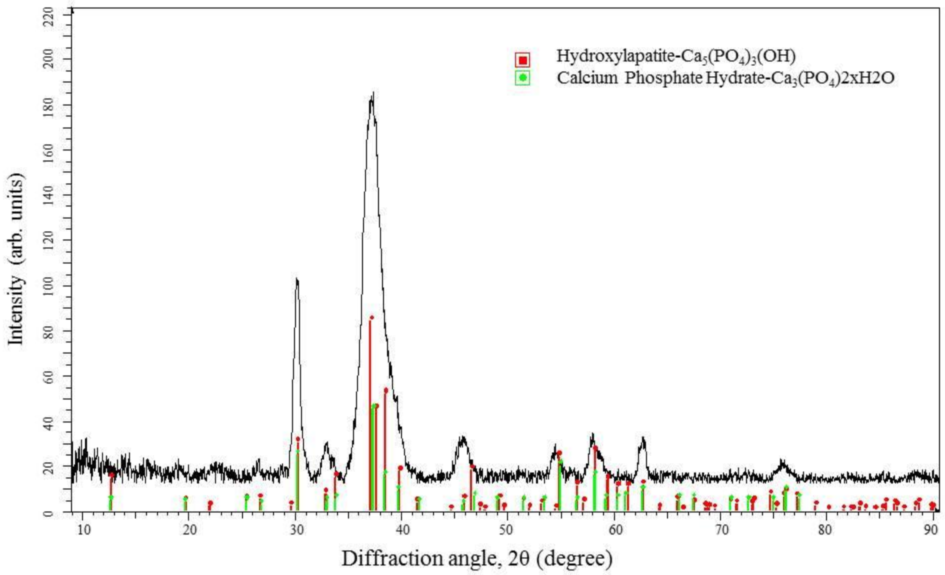

Figure 4. 3: X-ray diffraction pattern of precipitate collected from a control experiment compared to standard spectra for hydroxyapatite (red) and calcium phosphate hydrate (green).

4.3 Dynamic Light Scattering Results for nOPN

We examined the effect of nOPN on HA crystal nucleation and growth. The prepared solution contained 5.80 mM calcium and 3.63 mM phosphate ions. Figure 4.4 (A) shows the scattered intensity as a function of time for concentrations of 0, 1, 2, 3, 4, and 8 μg/ml nOPN. These concentrations correspond to approximately 0.03, 0.06, 0.08, 0.12, and 0.24 μM of nOPN. Here, the error bars for the scattered intensity indicate the standard deviation of the count rate. Adding 1 μg/ml nOPN notably decreases the scattered light intensity, and as the concentration of nOPN is increased, the scattered intensity drops further. From Figure 4.4 (B) we can see that the presence of nOPN causes a delay in nucleation and growth of the particles. The delay times become larger as the nOPN concentration increases.

Figure 4.4 (B) shows the mean hydrodynamic radius as a function of time for different concentrations of nOPN. The error bars on the plot of $\bar{r}_h$ versus time indicate the standard deviation of the distribution of the particle sizes, σ_r, which is found by fitting Equation (2.9) to the intensity autocorrelation function. At early times, $\overline{r_h}$ remains low and smaller than in the control experiment. After a delay, it finally starts to grow. Similar to what was observed for the scattered intensity, the presence of nOPN delays the growth of the particles, with the delay time becoming larger as the concentration increases. Once the crystals start to grow, they grow faster than in the control experiment, and eventually, the size of precipitating particles becomes larger than in the control experiment. In spite of this, the scattered intensity is always smaller than that of the control experiment. As described earlier, the scattered intensity depends on both the concentration and the size of the scatterers. Here, in the presence of nOPN, the size of the scattering particles increases but the scattered intensity remains lower than the control value. We can therefore infer that the concentration of the scattering particles decreases in the presence of nOPN. These results imply that nOPN inhibits the nucleation of the HA crystals. Very few calcium phosphate particles can nucleate when nOPN is added to the solution, but, as Figure 4.4 (B) shows, after a delay those particles grow faster in the presence of nOPN than in the control experiment.

Figure 4.4 (C) shows the scattered light intensity as a function of hydrodynamic radius. At a fixed size of scatterers, I_m depends only on the number of scattering particles. For sizes greater than about 200 nm, the number density of the scattering particles decreases significantly when protein is added to the solution. For instance, at 400 nm the value of I_m for 1 μg/ml nOPN is smaller than the control value by a factor of five. Overall, the results suggest that nOPN inhibits the nucleation of HA crystals.

The delay time was found by fitting a straight line to $\overline{r_h}(t)$ in a time interval just after it starts to grow significantly and then extrapolating the fit to $\overline{r_h} = 0$. Figure 4.5 illustrates that the delay time increases with concentration of protein. The dashed line, which is a linear fit to the data points, implies that there is a threshold concentration of 0.65±0.47 μg/ml for nucleating HA crystals in presence of nOPN.

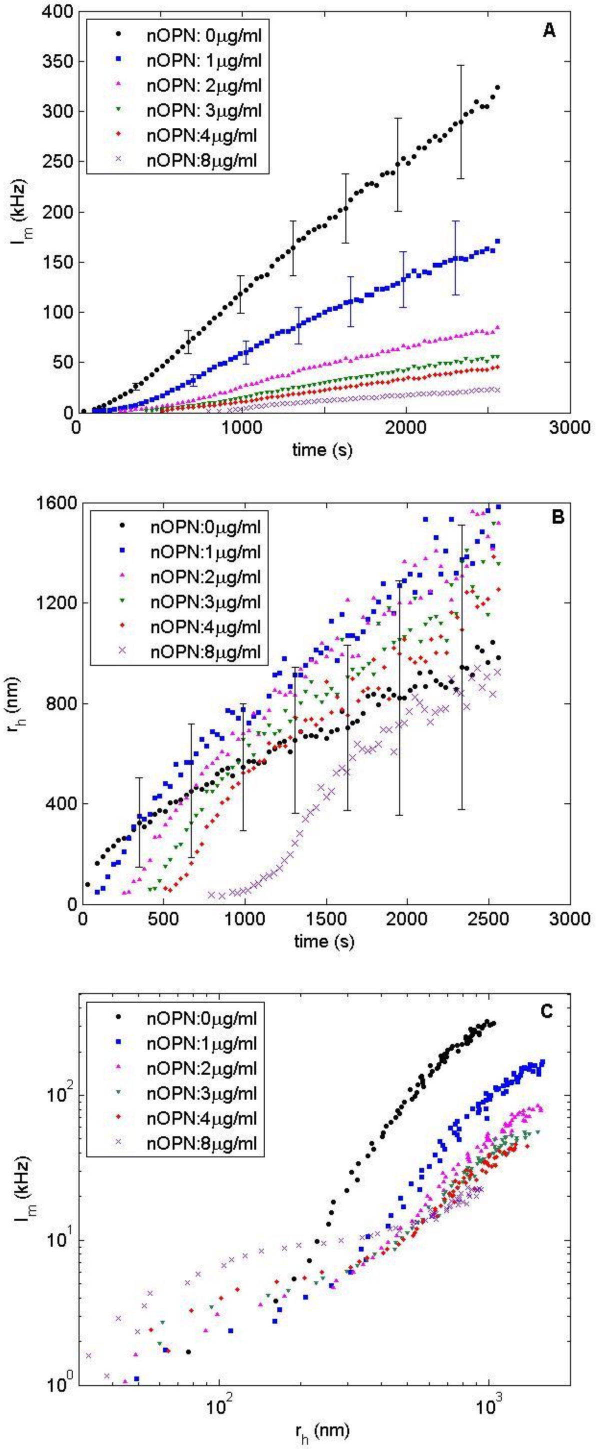

Figure 4. 4: (A) The mean scattered intensity versus time, (B) The mean hydrodynamic radius of the scatterers as a function of time, (C) The mean scattered photon count rate as a function of hydrodynamic radius in the presence of a range of concentration of nOPN added to the calcium phosphate solution.

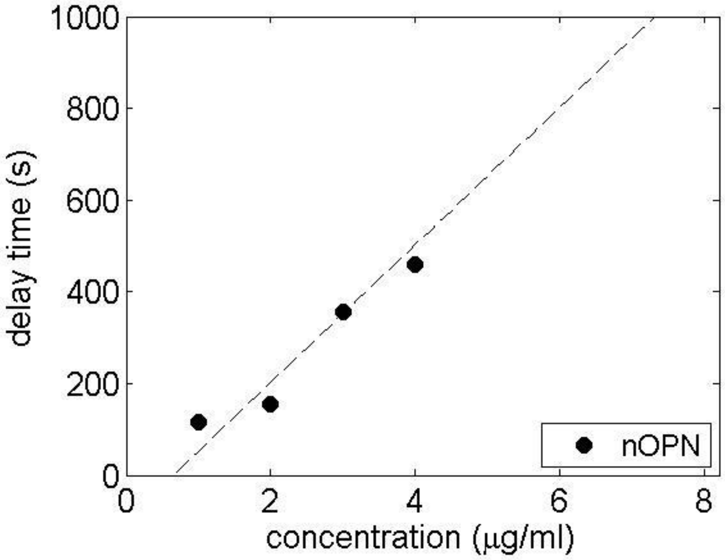

Figure 4. 5: Delay time as function of nOPN concentration for the beginning of the crystal growth.

4.4 Dynamic Light Scattering Results for rOPN

We studied the effect of recombinant OPN on the nucleation and growth of hydroxyapatite. Since rOPN lacks the phosphorylations of the native OPN, comparison of the results of these experiments with those of section 4.3 should provide information on the role of those phosphorylations on control of biomineralization.

Figure 4.6 (A) and (B) show the scattered photon count rate and the hydrodynamic radius of the scatterers in the presence of 1, 3, and 6 μg/ml rOPN. These concentrations correspond to approximately 0.03, 0.08, and 0.17 μM of rOPN. As in the case of nOPN, I_m decreases as the rOPN concentration increases but $\overline{r_h}$ behaves differently. $\overline{r_h}$ decreases as the concentration of rOPN increases with minimal apparent growth of particles at high concentrations. As the concentration increases from 1 μg/ml to 3 μg/ml the hydrodynamic radius drops significantly. At 6 μg/ml rOPN, the highest concentration studied, the particles grow very little over the duration of the measurement. By the end of the experiment, there is a 94% decrease in the radius of the scatterers in the presence of 6 μg/ml rOPN relative to the control measurement. Based on these observations, we can infer that rOPN strongly inhibits the growth of HA crystals.

The scattered light intensity is plotted as a function of $\overline{r_h}$ in Figure 4.6 (C). At small $\overline{r_h}$, I_m is considerably higher in the presence of rOPN than in the control experiment. Thus, we can infer that at a fixed size of scatterers, the concentration of calcium phosphate particles is larger in the presence of the protein than in the control solution.

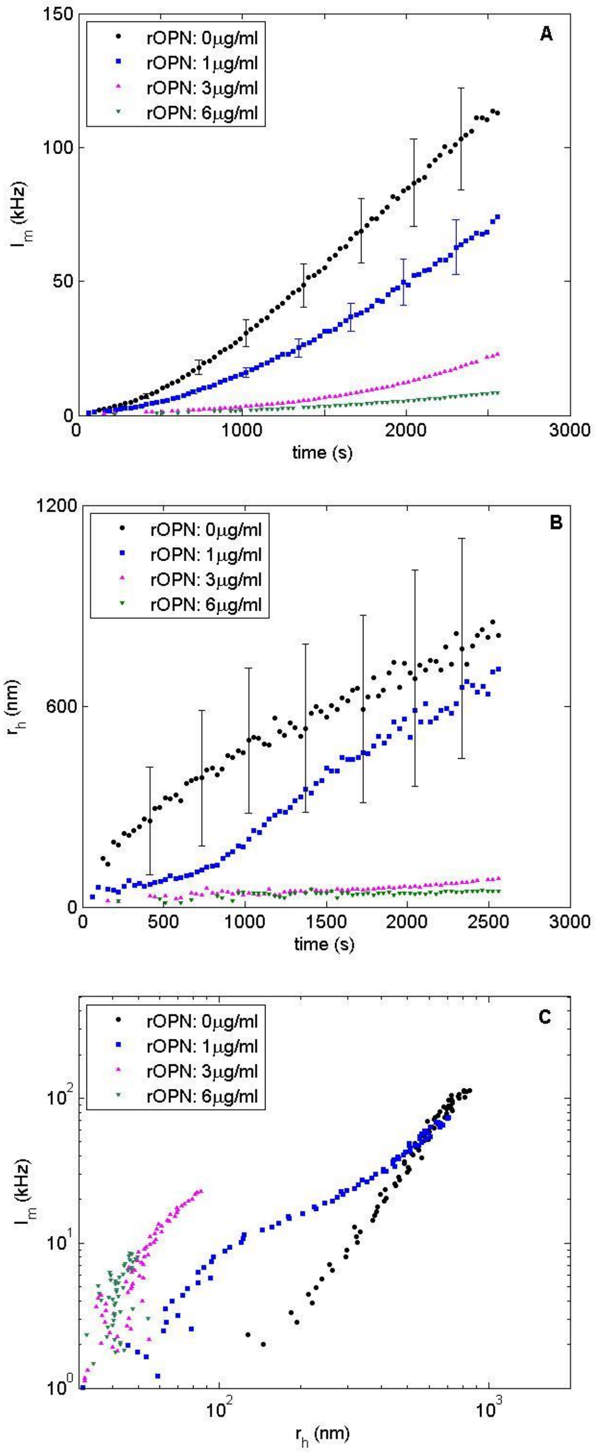

Figure 4. 6: Precipitation of calcium phosphate solution in the presence of recombinant OPN. (A) Mean scattered light intensity and (B) Mean hydrodynamic radius as a function of time for different concentration of rOPN. (C) Mean scattered light intensity as a function of hydrodynamic radiius.

4.5 X-ray Diffraction Results for nOPN and rOPN

Crystals were also harvested from experiments performed with 1 µg/ml nOPN and 1 µg/ml rOPN. The measured X-ray patterns are shown in Figures 4.7 and 4.8, respectively. Both samples have diffraction pattern features that match hydroxyapatite, ICDD card # 01-073-0293. As in the control experiment, the crystals formed in the presence of the proteins were very fine grained, as evidenced by broadening of the Debye rings in the powder pattern. Comparison of the X-ray diffraction patterns of the precipitants formed in the presence of nOPN and rOPN with that from the control experiment indicates that the patterns are similar, so the crystals formed are the same in all cases.

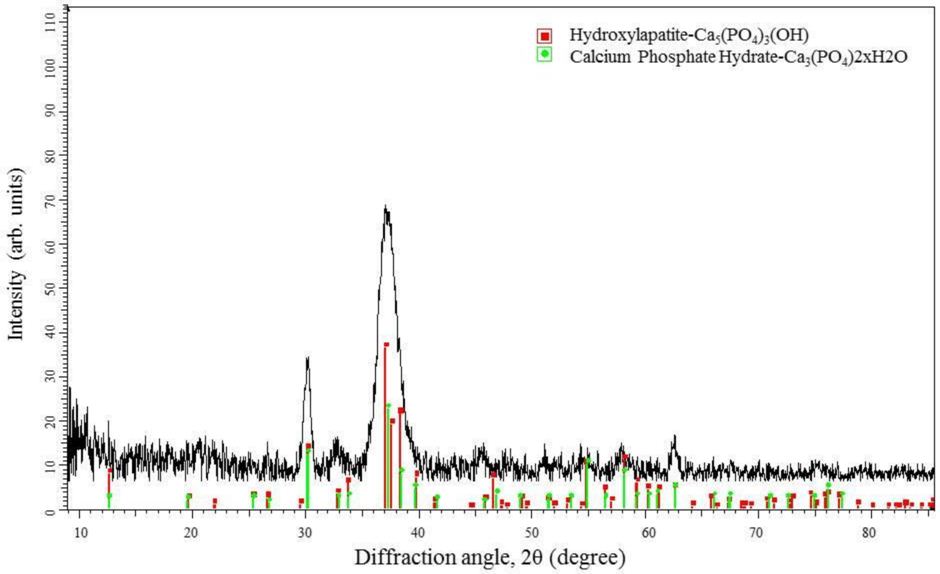

Figure 4. 7: X-ray diffraction pattern of precipitate collected from experiments in presence of 1 µg/ml nOPN.

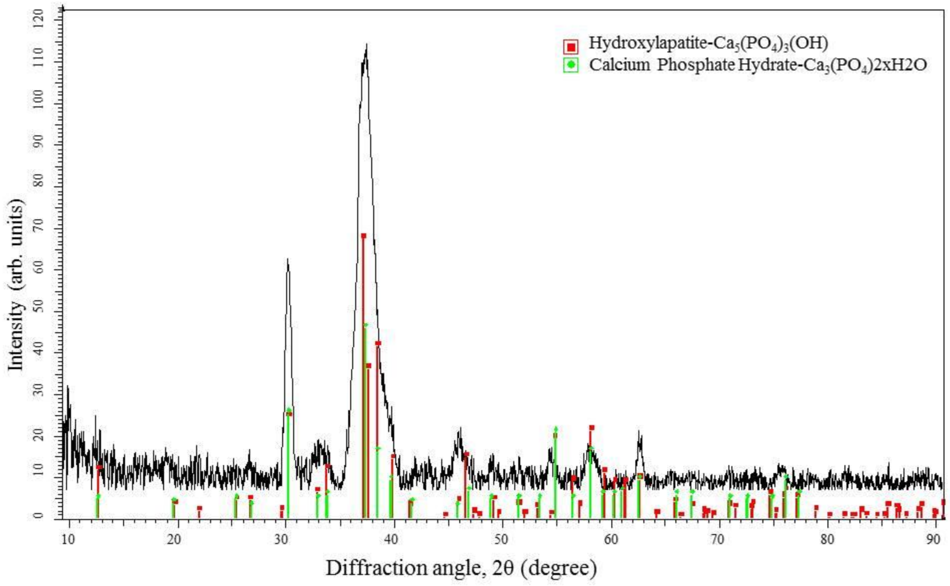

Figure 4. 8: X-ray diffraction pattern of precipitate collected from experiments in presence of 1 μg/ml.

4.6 Dynamic Light Scattering Results for P0

In vivo and *in vitro* studies have shown that OPN inhibits the nucleation and growth of HA and other biominerals and prevents the calcification of soft tissues. However, the nature of the interaction between OPN and HA is not yet fully understood. We performed experiments on peptides derived from OPN to investigate the inhibitory effects of particular regions of the protein. P0 is a non-phosphorylated peptide corresponding to amino acids 220-235 from OPN. Aliquots of 5, 7, 10 and 15 μg/ml of P0 were added to a solution with ion concentrations of 5.46 mM calcium and 3.41 mM phosphate. These peptide concentrations correspond to molar concentration of 3.0, 4.0, 6.0 and 9.0 μM, respectively. The results for P0 are presented in Figure 4.9.

As can be observed in Figure 4.9 (A), increasing the concentration P0 has only a small effect on the scattered light intensity. For the highest concentration of P0, 15 μg/ml, the average scattered light intensity at the end of the experiment decreases by 22% relative to the control level.

Figure 4.9 (B) demonstrates that hydrodynamic radius measured at peptide concentrations of 5, 7, and 10 μg/ml overlaps with the control data. Addition of 15 μg/ml of P0 to the solution causes the hydrodynamic radius to decrease slightly below the level of the control. These observations indicate that P0 has a very weak effect on HA formation, and inhibits crystal growth only at very high concentrations. Figure 4.9 (C) shows the intensity as a function of hydrodynamic radius. The scattered intensity at a given hydrodynamic radius in the presence of 5, 7, and 10 μg/ml peptide is slightly below the control experiment, indicating a small decrease in the concentrations of scatterers. At a concentration of 15 μg/ml, *I(t)* is slightly higher than in the control run, suggesting that at very high concentrations of P0, the number density of the calcium phosphate particles increases by a small amount. Overall, this peptide exhibits a very weak inhibitory effect on the growth of HA crystals.

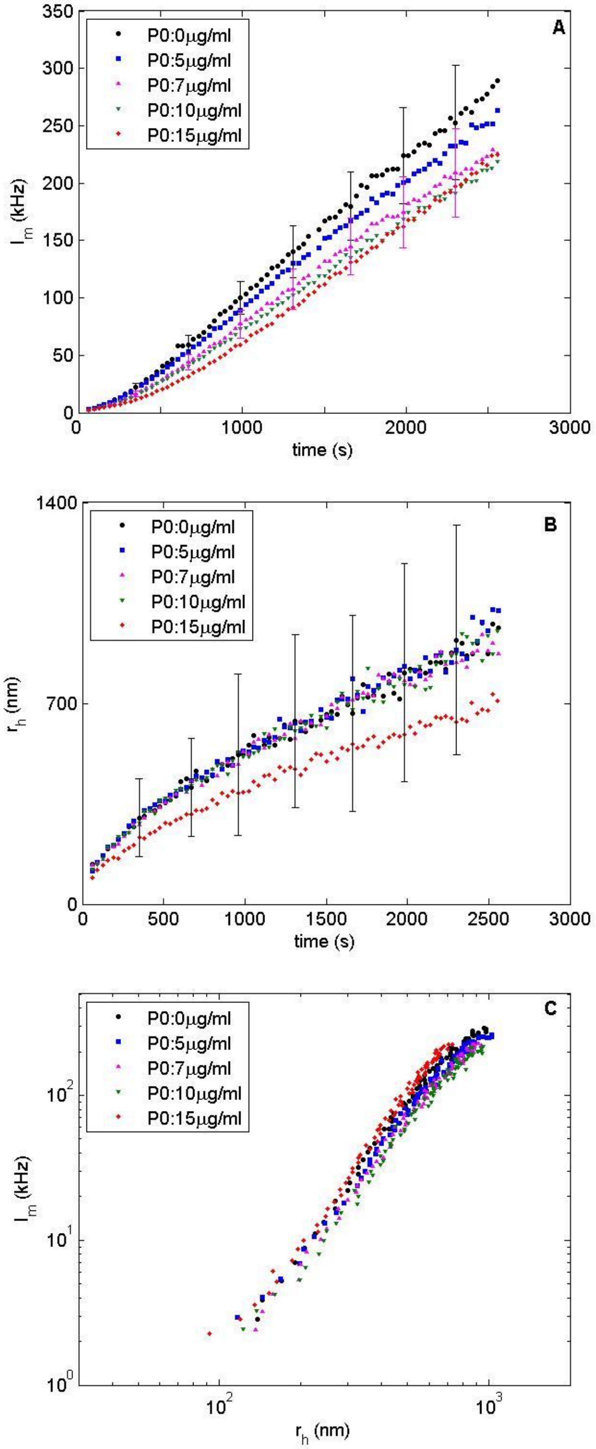

Figure 4. 9: (A) Mean scattered light intensity as a function of time, (B) mean hydrodynamic radius as a function of time, (C) scattered light intensity as a function of hydrodynamic radius for different concentration of P0.

4.7 Dynamic Light Scattering Results for P3

The inhibitory effect of P3, which is a synthetic peptide containing 3 phosphates corresponding to OPN sequence 220-235, was measured using dynamic light scattering. We added 0.3, 0.5, 1, 2, and 5 μg/ml P3 to a calcium phosphate solution that contained 5.40 mM Ca^{2+} and 3.37 mM PO_4^{3-}. The P3 concentrations correspond to approximately 0.15, 0.25, 0.50, 1.0, and 2.50 μM, respectively. In contrast to P0, the inhibitory effect of P3 was observable at relatively low concentrations.

As illustrated in Figure 4.10 (A), the presence of P3 causes the scattered intensity to drop, with the count rate becoming lower as the concentration of P3 increases. At the highest studied concentration of the peptide, 5 μg/ml, the mean scattered light intensity at the end of the measurement shows an approximate ten-fold reduction relative to the control experiment.

The effect of P3 on $\overline{r_h}$ is presented in Figure 4.10 (B). It shows that increasing the concentration of P3 has no measurable effect on the hydrodynamic radius of HA crystals. For the highest concentration of P3, the hydrodynamic radius at the end of the experiment decreases by 4.7% relative to the control level. No delay in crystal growth was observed in the presence of P3.

The scattered light intensity as a function of the hydrodynamic radius is shown in Figure 4.10 (C). As the figure illustrates, all concentrations of P3 reduce the photon count rate below the level of the control at any given hydrodynamic radius. The addition of increasing concentration of P3 resulted in decreased concentration of HA crystals. Altogether, P3 is a potent inhibitor of HA nucleation.

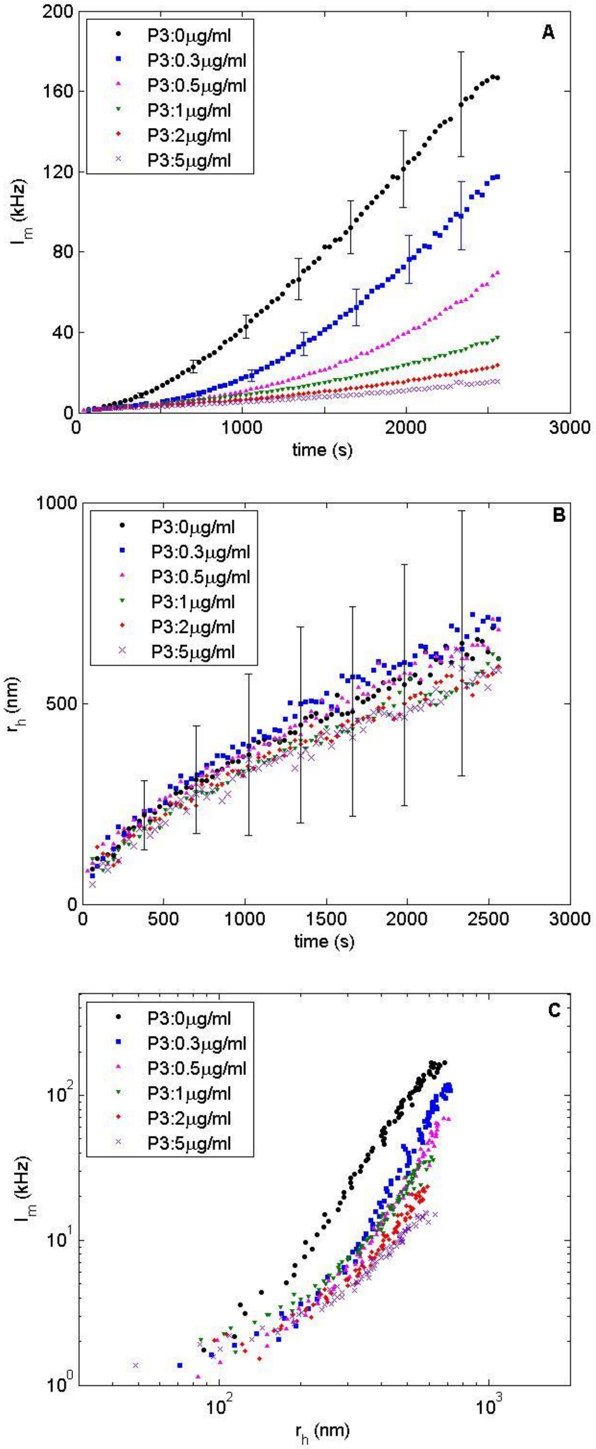

Figure 4. 10: (A) Mean scattered light intensity as a function of time, (B) mean hydrodynamic radius as a function of time, (C) scattered light intensity as a function of hydrodynamic radius for different concentrations of P3.

4.8 Dynamic Light Scattering Results for OPAR

We also studied the effects of other OPN-derived synthetic peptides on HA growth. A peptide corresponding to the Osteopontin Poly-Aspartate Region (OPAR; OPN65-80) was incubated with a calcium phosphate solution containing 5.66 mM calcium and 3.53 mM phosphate ions.

Figure 4.11 (A) shows the plot of the scattered photon count rate as a function of time in the presence of different concentrations of OPAR. The OPAR concentrations studied were 0.3, 0.5, 1, 2, 5 and 7 μg/ml, corresponding to approximately 0.16, 0.3, 0.55, 1.1, 2.7, and 4.0 μM, respectively. Error bars are analogous to those in previous figures. The intensity of the scattered laser light starts to drop immediately and without any delay as we add OPAR to the calcium phosphate solution. I_m increases roughly linearly over the course of measurement and decreases as the OPAR concentration increases. With 7 μg/ml of OPAR added to the calcium phosphate solution, the intensity at the end of the measurement was decreased by a factor of six.

Figure 4.11 (B) shows the mean hydrodynamic radius of the particles as well as the standard deviation of particle sizes. Regardless of the peptide concentrations, the HA crystals grow in a similar manner. At the beginning of the measurement, the sizes of the particles are more or less the same for all concentrations. It seems the particles are slightly smaller when OPAR is added, but the difference from the control is small. The fact that particles have sizes almost the same as the control solutions combined with their lower value for the scattered intensity, suggest that the concentration of the particles has decreased in the presence of OPAR. No delay in crystal growth is observed. These results suggest that the presence of OPAR significantly inhibits nucleation but not growth. Results for I_m as a function of hydrodynamic radius are shown in Figure 4.11 (C). At small fixed sizes and in the presence of the lowest protein concentration, the particles scatter light as much as they do in the control experiment. As the concentration of OPAR increases, the photon count rates decreases. At about 300 nm size, the scattered intensity drops by about a factor of six for the highest OPAR concentration studied, 7 μg/ml. Since the addition of OPAR to the calcium phosphate solution decreases the concentration of the precipitant, these findings suggest that OPAR is a moderate inhibitor of nucleation.

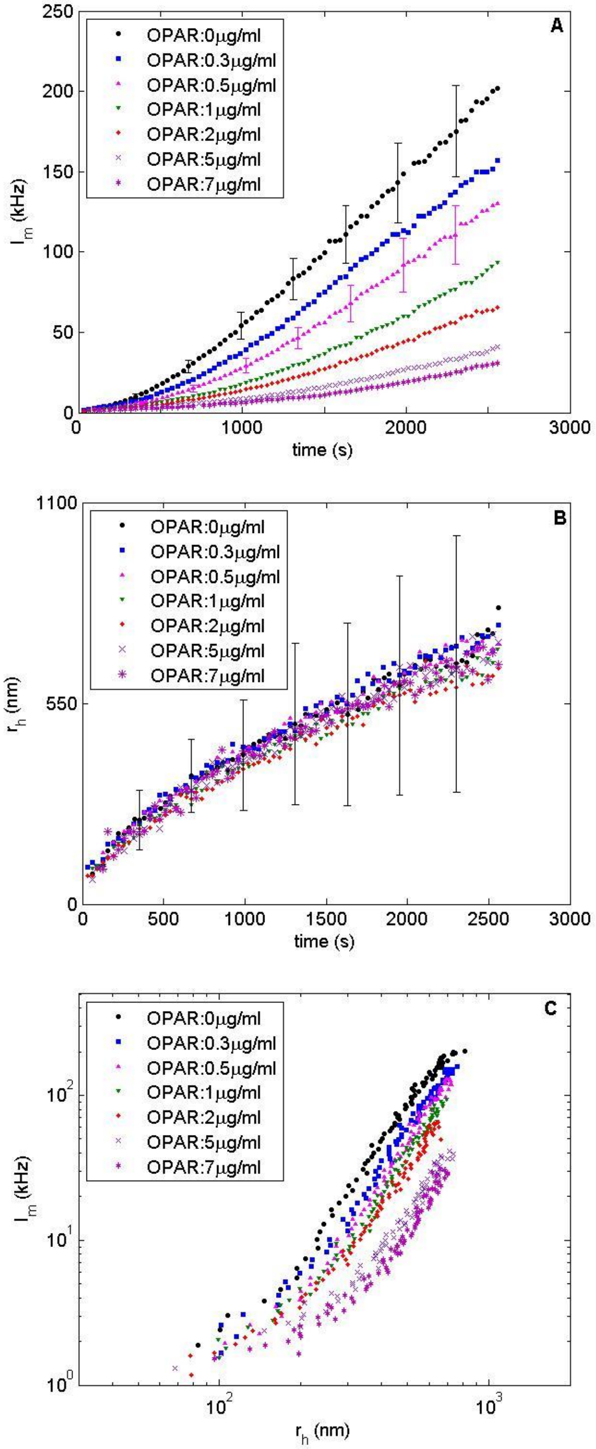

Figure 4. 11: (A) Mean scattered light intensity as a function of time, (B) mean hydrodynamic radius as a function of time, (C) scattered light intensity as a function of hydrodynamic radius for different concentrations of OPAR.

4.9 Dynamic Light Scattering Results for pOPAR

We also used DLS to measure the size and growth rate of crystals precipitating from a solution of calcium phosphate ions in the presence of the phosphorylated version of the osteopontin poly-aspartate region (pOPAR). We added 0.3, 0.5, 1, and 2 µg/ml pOPAR to a calcium phosphate solution that contained 5.73 mM Ca^{2+} and 3.58 mM PO_4^{3-}. The pOPAR concentrations correspond to approximately 0.15, 0.26, 0.52, and 1.05 µM, respectively.

The average scattered light intensity is plotted as a function of time for various concentrations of pOPAR in Figure 4.12 (A). The photon count rate is slightly lower than in the case of OPAR, however, the overall behaviour is almost the same. Increasing the concentration of pOPAR decreases the photon count relative to the control measurement.

The effect of pOPAR on the hydrodynamic radius is presented in Figure 4.12 (B). It shows that the size of the particles in the presence of pOPAR is slightly smaller than in control over the course of measurement. At all studied pOPAR concentrations, the growth rates of the precipitating crystals are similar to each other and to the control. Furthermore, no delay in the growth of these calcium phosphate particles is observed.

The effect of pOPAR concentration becomes more evident if the average scattered light intensity as a function of hydrodynamic radius is plotted. Figure 4.12 (C) illustrates that at a particular size of the scatterers, I_m decreases as the amount of the peptide is increased, meaning that the number density of the HA particles becomes lower as the pOPAR concentration is increased. In the presence of pOPAR, few particles form at early times but they grow at the same rate as in the control experiment. Fewer particles imply that pOPAR reduced the level of nucleation of HA. Since in the presence of pOPAR the crystals become slightly smaller, pOPAR may also have a small effect on the growth of the hydroxyapatite crystals.

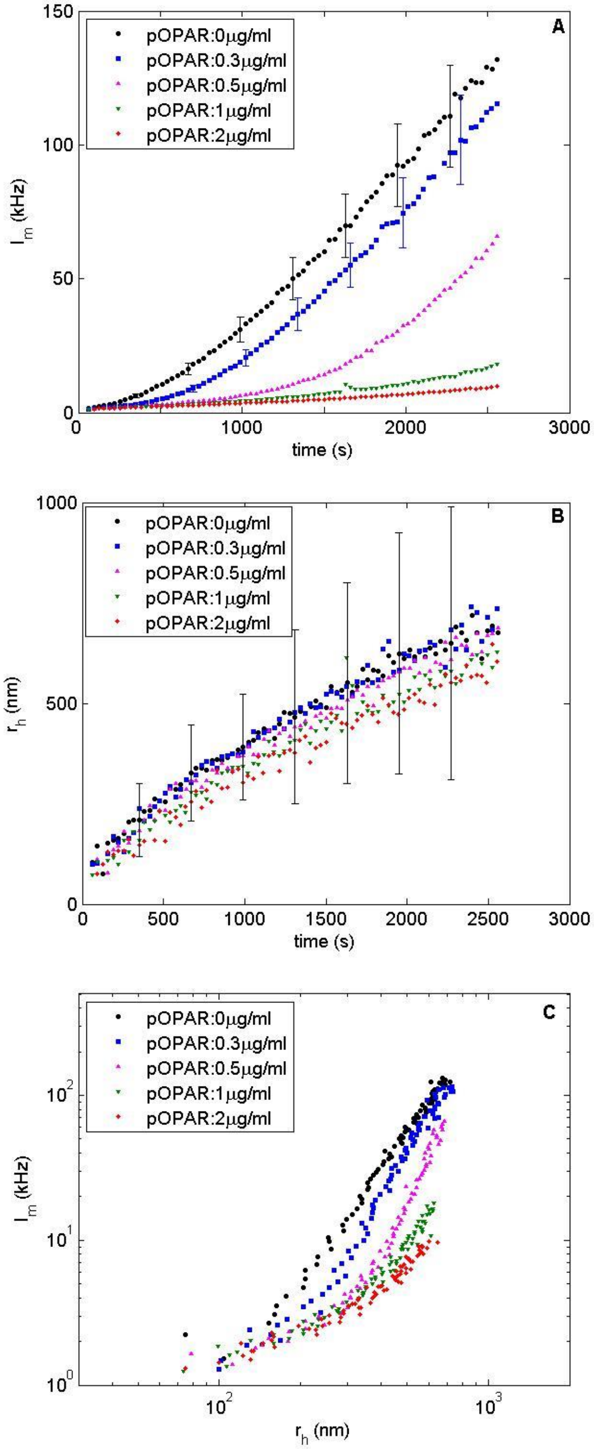

Figure 4. 12: (A) Mean scattered light intensity as a function of time, (B) mean hydrodynamic radius as a function of time, (C) scattered light intensity as a function of hydrodynamic radius for different concentrations of pOPAR.

4.10 Dynamic Light Scattering Results for rBSP

It has been proposed that BSP acts to initiate calcification in mineralized tissues [20,47]. To test this hypothesis, the effect of recombinant BSP on hydroxyapatite crystal formation was measured using dynamic light scattering. We attempted to find a concentration of calcium and phosphate ions at which precipitation of crystals does not happen in the absence of rBSP, but did happen in the presence of rBSP. It was postulated that BSP would cause the spontaneous nucleation of crystals below the normal threshold concentrations of calcium and phosphate ions.

We studied the effect of adding protein on two solutions with different concentrations of calcium and phosphate. The first solution contained 5.20 mM Ca^{2+} and 3.25 mM PO_4^{3-} and the second solution contained slightly higher calcium and phosphate ion concentrations: 5.40 mM Ca^{2+} and 3.37 mM PO_4^{3-}.

Figures 4.13 (A) and (B) show the scattered intensity and the hydrodynamic radius as a function of time for precipitation from the first solution for a control experiment and in the presence of 1, 2, 4 and 6 µg/ml rBSP, corresponding to molar concentrations of approximately 0.03, 0.06, 0.12, and 0.18 µM rBSP. The scattered photon count rate is very low for this solution, indicating a low concentration of scatterers. As can be observed from Figure 4.13 (A), at an rBSP concentration of 1 µg/ml, the average scattered light intensity is above the level measured in the control experiment; at 2 µg/ml rBSP, the scattered intensity is initially lower but becomes equivalent to the control experiment at 40 minutes. At higher rBSP concentrations, I_m is decreased throughout the 40 minute duration of the experiment. Figure 4.13 (B) shows that for all concentrations studied, the particles are smaller than in the control experiment. Increasing the concentration of rBSP decreases the size of the crystals at any given time. This suggests that rBSP at 1 and 2 µg/ml enhance nucleation.

As mentioned above, for a concentration of 1 µg/ml the scattered intensity is higher than the control value, but the hydrodynamic radius is smaller. I_m depends on both the size as well as the concentration of the scatterers. Since I_m is higher than the control value for 1 µg/ml, while $\overline{r_h}$ is smaller we can infer that the concentration of the calcium phosphate particles has increased in the presence of low protein concentration. For concentrations of 4 and 6 µg/ml, few particles are detected within the first 1500 seconds of the experiment, and then the particles that do form grow slowly over the duration of the measurement. At the end of the experiment there is about a four-fold reduction in $\overline{r_h}$ for 2 µg/ml rBSP compared to the control, though the scattered intensity is equivalent. This indicates that the concentration of the particles is increased compared to the control at 40 minutes, suggesting that at low protein concentration rBSP enhances nucleation.

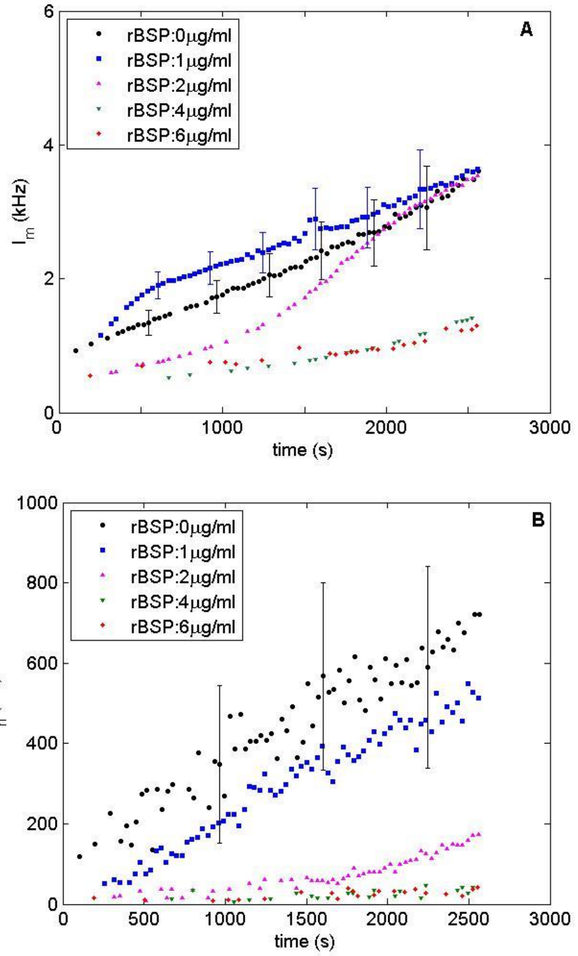

Figure 4. 13: (A) The mean scattered intensity versus time, and (B) The mean hydrodynamic radius of the scatterers as a function of time, for experiments in which rBSP is added to the 5.20 mM calcium and 3.25 mM phosphate solution.

This experiment was done only once. The results may be affected by small uncertainties in concentration due to pipetting uncertainties. More trials would be needed to allow a definitive conclusion. Nonetheless, our data suggest that rBSP enhances nucleation at low concentrations, while it appears to inhibit growth at 2 µg/ml and higher.

This experiment was repeated with the higher-concentration solution containing 5.40 mM Ca^{2+} and 3.37 mM PO_4^{3-}. The measured scattered photon count rate and the size of the particles are shown in Figure 4.14 (A) and (B). Based on the control data, at these ion concentrations there is substantial crystal formation in the absence of protein. Experiments were performed with 1, 2, 4, 6, and 8 µg/ml of rBSP added to the solution, corresponding to molar concentrations of approximately 0.03, 0.06, 0.12, 0.18, and 0.23 µM.

Adding 1 µg/ml rBSP to the solution does not have a significant effect on the scattered light intensity. For higher concentrations, however, I_m decreases as the rBSP concentration increases. The scattered light intensity has almost the same value for the two highest concentrations studied.

The effect of rBSP on calcium phosphate precipitation at supersaturated concentrations of calcium and phosphate is similar to that observed with the addition of OPN, though the inhibition is markedly less. At 1 µg/ml rBSP, there is little change in I_m compared to the control experiment, but at higher concentrations of rBSP, I_m decreases (Fig 4.14 (A)). At 8 µg/ml, rBSP reduces I_m by 50% whereas 8 µg/ml of nOPN (Figure 4.4 (A)) and 6 µg/ml of rOPN (Figure 4.6 (A)) reduces I_m by 90% or more. Increasing the concentration of rBSP appears to cause a short delay in the increase of the scattered intensity, but, again, this effect is much less than that observed with both isoforms of OPN.

Similar to what is observed for nOPN, once the particles begin to grow, the hydrodynamic radius increases more quickly in the presence of the protein than in the control experiment. After 1000 seconds, the precipitating particles are actually larger than in the control experiment. However, it is not clear that rBSP causes a true delay in nucleation, since particle formation is observed at early times for all concentrations of rBSP tested. In contrast, the data for nOPN showed a more distinct absence of particle formation at early times.

To better distinguish the effect of rBSP on the HA crystal concentration, the scattered light intensity is plotted as a function of mean hydrodynamic radius in Figure 4.14 (C). At small values of $\overline{r_h}$, for high concentration of rBSP I_m is higher in the presence of the protein suggesting that rBSP promotes the formation of small particles. For $\overline{r_h}$ greater than about 300 nm, however, the scattered light intensity is lower in the control experiment, suggesting fewer particles of larger size in the presence of the protein. The $\bar{r}_h$ vs. time data show that these particles grow faster than in the control experiment. The scattered intensity initially decreases as rBSP concentration increases, then appears to increase again for the highest rBSP concentrations studied. This will be discussed further in the Chapter 5.

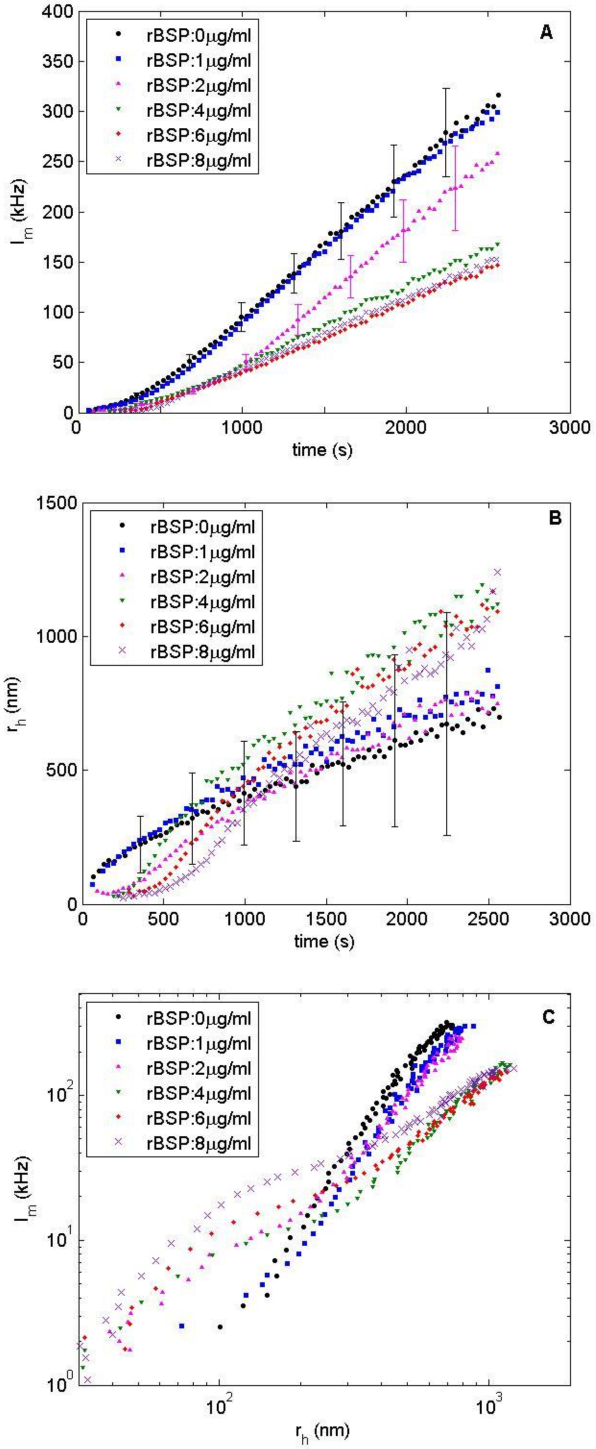

Figure 4. 14: (A) The mean scattered intensity versus time, (B) the mean hydrodynamic radius of the scatterers as a function of time, (C) the mean scattered intensity as a function of hydrodynamic radius for rBSP added to a solution containing 5.40 mM calcium and 3.37 mM Phosphate.

Chapter 5: Discussion

Dynamic light scattering is a well-established, versatile and non-invasive technique which can provide information about the size distribution of the scatterers and particle populations in real time. Dynamic light scattering has long been a powerful tool for studying a wide range of phenomena. It offers an alternative approach to the study of the protein-biomineral interactions. In the work described in this thesis, we have used DLS to investigate the kinetics of the nucleation and growth of crystals from a supersaturated solution of calcium and phosphate ions in the presence of bone-related proteins and synthetic peptides. Unlike the traditional methods described in sections 1.4.1 and 1.4.2, DLS permits us to monitor the initial stages of the nucleation process and determine the size and relative concentration of the growing crystals as a function of time. This allows an immediate assessment of the effect of proteins on mineralization and nucleation.

BSP has been shown previously to act as a nucleator of HA crystallization [20,47]. We attempted to study this phenomenon using DLS, but found that studying nucleation is not as simple as studying inhibition. It was particularly difficult to find a threshold ion concentration at which adding BSP triggers the formation of HA. We attempted to find the critical point at which $CaPO_4$ will not precipitate in the absence of BSP, but at which addition of BSP will result in biomineral nucleation. We modified the experimental solution changing the concentrations of salts and buffers. Unfortunately, we were unable to find a concentration at which BSP unambiguously caused nucleation. Poly glutamic acid, which has also been shown to be a potent driver of nucleation [84], was also not observed to induce nucleation in this system. Because of this we decided to change our approach and did not focus on the nucleation effects of BSP below the threshold for HA formation, but rather studied inhibitory proteins and peptides above the nucleation threshold.

5.1 Osteopontin

Our results show that both native and recombinant OPN inhibit the precipitation of calcium phosphate particles from solution. Native OPN delays the nucleation of particles and causes a significant decrease in particle concentration compared to the control experiment. However, the few calcium phosphate particles that do nucleate grow faster than in the control experiment. At the end of the measurement, the mean particle size is greater than 1 μm. The time at which $\bar{r}_h$ starts to grow significantly increases linearly with the concentration of nOPN. In the presence of OPN, the scattered light intensity is significantly below that of the control experiment, indicating that the number density of scattering particles has decreased. We can therefore conclude that the presence of nOPN strongly prevents the formation of the particles. This could have occurred in two ways: the nOPN could inhibit the nucleation of calcium phosphate particles, or it could prevent small nucleated clusters from growing large enough to be observed by the DLS detector.

In the presence of rOPN, both the scattered light intensity and the size of particles decrease. Moreover, the particles grow more slowly than in the absence of protein. In contrast to the case of nOPN, rOPN does not cause any noticeable delay in early precipitation. We can thus infer that rOPN does not have any effect on the nucleation of calcium phosphate particles but it slows their growth.

In vitro studies have indicated that OPN and natural and synthetic OPN peptides are strong inhibitors of nucleation [23,24,38] and growth [39] of HA crystals. Although the mechanism by which mineral formation and growth are inhibited is poorly understood, other studies have shown that OPN also inhibits the formation of other biominerals, such as calcium carbonate [37] and calcium oxalate [41,42]. Hunter and co-workers [38] found that modification of OPN's glutamic acid and aspartic acid residues reduces its inhibitory potency [38]. Constant composition studies, which measured seeded crystal growth, indicate that aspartic acid is a more effective inhibitor than glutamic acid [38]. It has also been demonstrated that the inhibition of crystal formation and growth by OPN involves an interaction between the contiguous aspartic acid segment of OPN and an array of lattice ions on the surface of the HA crystal [43,50].

Grohe et al. found that phosphate groups had a significant role in bringing the peptide close to the crystal surface. They simulated three forms of the same OPN peptide (P0, P1, P3), which have the same amino acid sequence but different numbers of phosphorylations, interacting with a calcium oxalate monohydrate (COM) crystal face. They suggested that the adsorption of acidic peptides to the {100} face of these biominerals is governed by electrostatics and is not dependent on the particular amino-acid sequence [30]. Another group performed simulations on phosphorylated OPN peptides in the presence of calcium oxalate, and also concluded that phosphate groups are involved in the inhibition of crystal growth [46]. Therefore, phosphate groups increase the electronegativity of OPN, causing a strong interaction with positively charged crystal face.

Phosphorylation plays a key role in OPN's mineral-modulating activity, with phosphorylated OPN or its related peptides being much more inhibitory than the non-phosphorylated recombinant peptides [38,45,46].

More recently de Bruyn et al. applied dynamic light scattering to characterize the effects of proteins on mineral formation. To evaluate the effect of PTMs, three isoforms of OPN – nOPN, rOPN and phosphorylated rOPN (p-rOPN) – were examined. Their investigation showed that both nOPN and p-rOPN inhibit the nucleation of particles from supersaturated calcium phosphate solutions. On the other hand, rOPN, which lacks the phosphorylations of nOPN, acted as an inhibitor of HA growth but not the nucleation [75].

Although phosphorylation of OPN seems to be essential to its capability to prevent mineral growth, it is not clear whether phosphorylation at particular sites in the protein is needed. In this thesis, we addressed this issue by testing some OPN-derived peptides for their effect on HA formation and growth. There is some overlap with the work done by de Bruyn and co-workers [75], and in such cases our results are in good agreement with theirs.

The growth rate of the precipitating crystals in the presence of nOPN and rOPN are plotted as a function of protein concentration in Figure 5.1. A straight line was fitted to the hydrodynamic radius data from each run at the time when the hydrodynamic radius was 200 nm. The growth rate increases with [nOPN], while rOPN causes it to decrease. The decrease in growth rate, combined with the absence of a delay in precipitation, suggests that rOPN inhibits the growth, but not the nucleation of HA crystals.

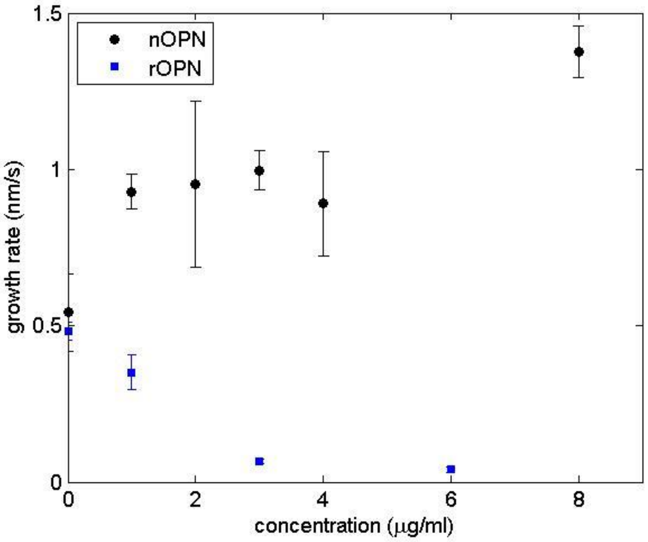

Figure 5. 1: Growth rate as a function of concentration for nOPN and rOPN at

$\bar{r}_h = 20\ 0nm.$

5.2 Quantitative Comparison of Peptides

The experiments were performed on different days with slightly different concentrations. To compare the results obtained for the different OPN-related peptides, the data for the hydrodynamic radius of precipitating particles were normalized over time with respect to the control data. The control data were fitted to a cubic polynomial. Figure 5.2 (A) shows $\overline{r_h}$ data from a typical control run with the fitted polynomial. The deviations of the data from the fit are illustrated in Figure 5.2 (B). For normalization, the hydrodynamic radius from the peptide run is divided by the fitted value of $\overline{r_h}$ for the control at the same time.

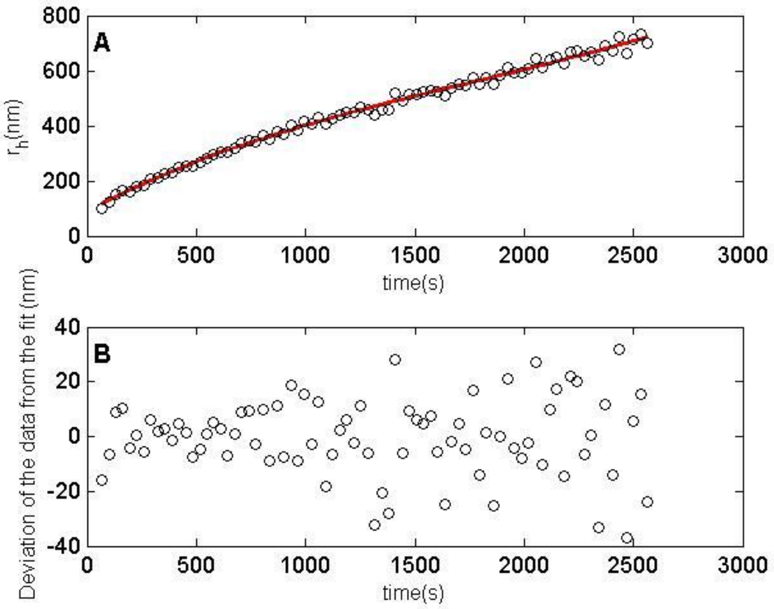

Figure 5. 2: (A) Typical data for the hydrodynamic radius in a control run. The red line is a fit to a cubic polynomial. (B) The deviations of the data from the fit.

To compare the inhibitory effects of OPN-related peptides, their hydrodynamic radius data were normalized as described, then averaged over time.

Figures 5.3 (A) and (B) show the mean normalized hydrodynamic radius as a function of concentration for P0 and P3 respectively. At low concentrations, P0 has no discernible effect on the growth of the HA crystals, but the normalized hydrodynamic radius decreases in the presence of a high concentration of P0.

Increasing the concentration of P3 decreases the hydrodynamic radius substantially. At a concentration of 5 μg/ml, P0 does not have a measurable effect on the mean normalized hydrodynamic radius over the forty-minute incubation, while the same concentration of P3 results in a 15% decrease in the mean normalized hydrodynamic radius. This indicates that the three phosphate groups on P3 play a major role in the inhibition of HA growth.

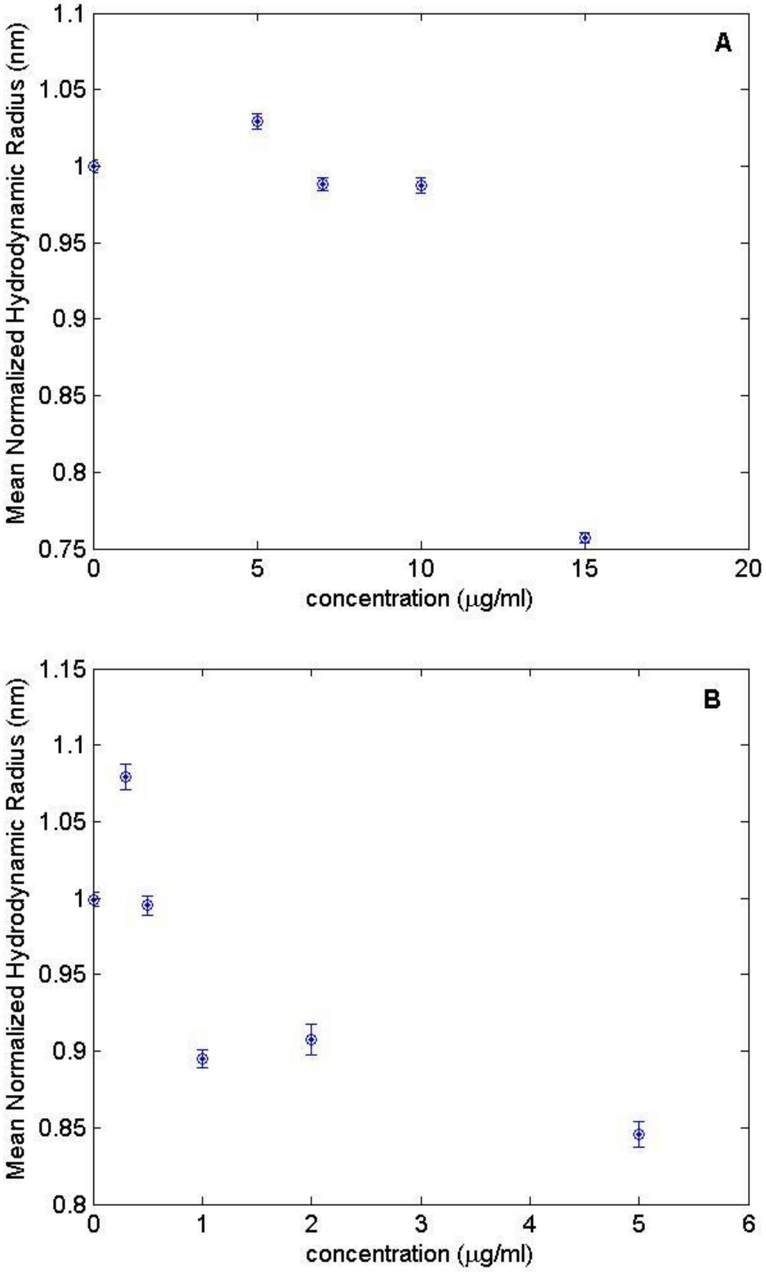

Figure 5. 3: Mean normalized hydrodynamic radius as a function of concentration for A) P0 and B) P3.

The growth rate of the precipitating crystals in the presence of P0 and P3 is plotted as a function of concentration in Figure 5.4. The growth rate was determined by fitting a straight line to the hydrodynamic radius data for each run at the time when the hydrodynamic radius was 200 nm. The growth rate for both peptides decreases with increasing concentration, but the effect is much more pronounced for P3. This result also indicates that the three phosphates on the P3 peptide increase its inhibition potency relative to that of P0.

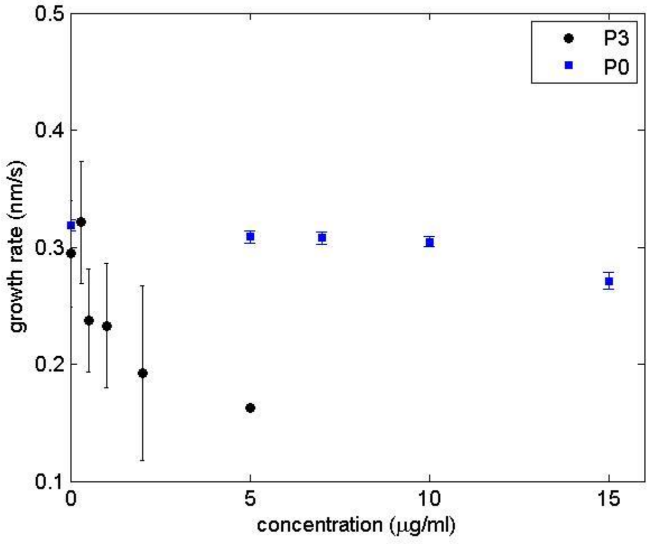

Figure 5. 4: Growth rate as a function of concentration for P0 and P3 at

$\bar{r}_h = 20\ 0nm$.

The mean normalized hydrodynamic radius for OPAR and pOPAR are plotted versus concentration in Figures 5.5 (A) and (B) respectively. These two peptides, which differ only by the phosphate group on pOPAR, both moderately inhibit the growth of HA crystals at concentrations up to 2 μg/ml. At higher concentrations of OPAR, the mean value of the normalized hydrodynamic radius increases back to the control value. This behaviour is not understood but suggests that the inhibitory potency of OPAR is somehow neutralized at high concentrations.

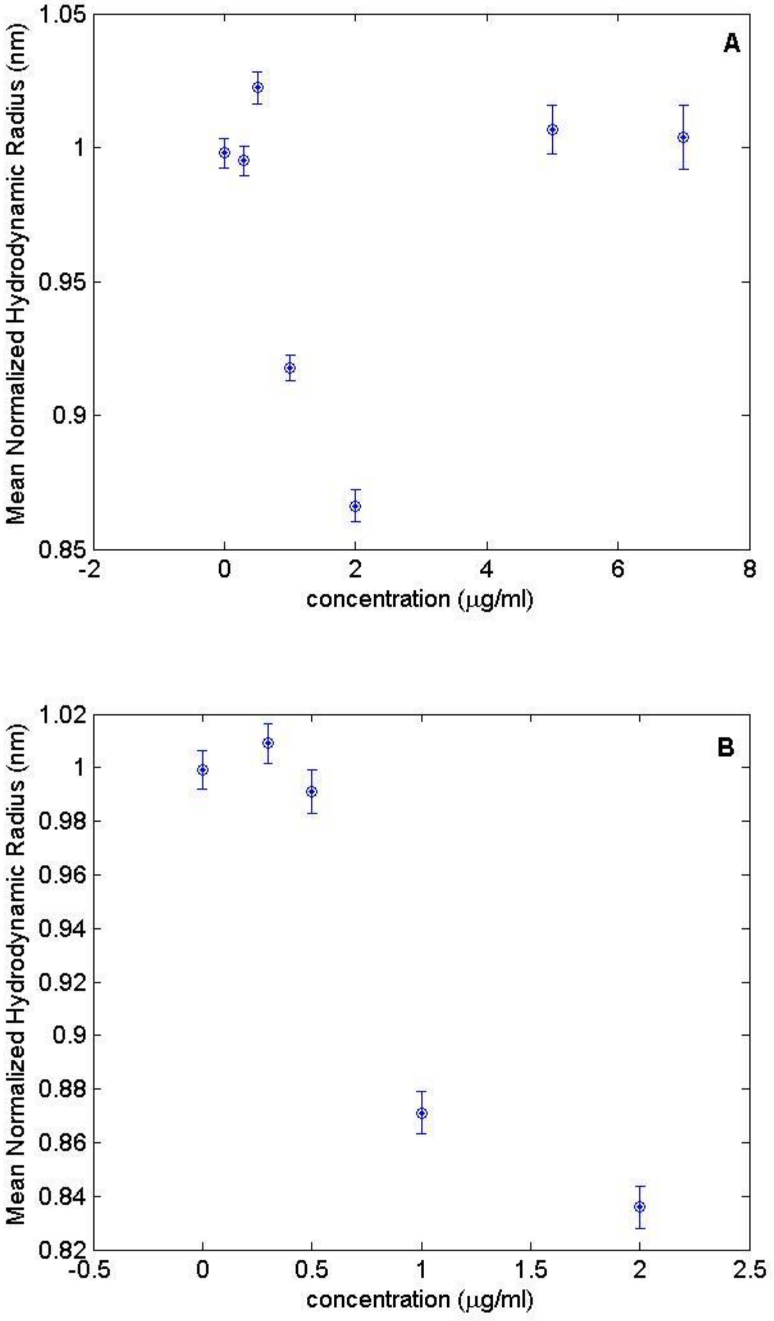

Figure 5. 5: Mean normalized hydrodynamic radius as a function of concentration for A) OPAR and B) pOPAR.

Figure 5.6 shows the same data for both peptides at low concentrations. Up to 2 μg/ml both peptides have roughly the same inhibitory effect on HA growth but the mean normalized hydrodynamic radius is slightly smaller for pOPAR. This suggests that the aspartic acid groups in both peptides cause inhibition, but also that the extra phosphate on the pOPAR increases its inhibitory effect.

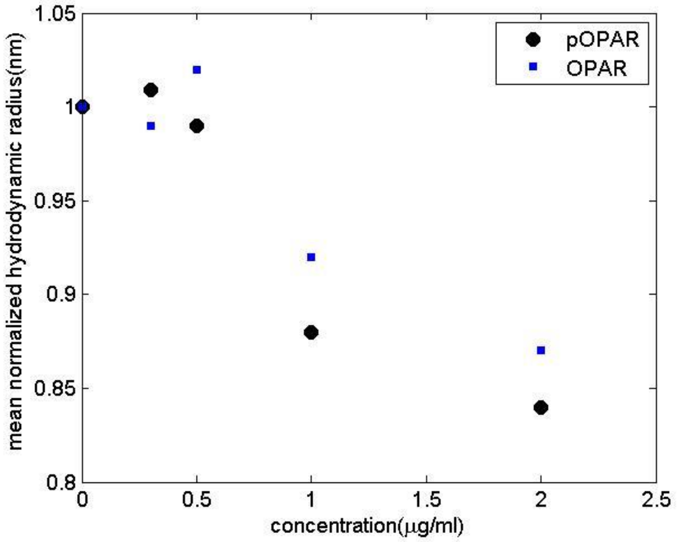

Figure 5. 6: Mean normalized hydrodynamic radius as a function of concentration for OPAR and pOPAR.

The growth rate as a function of concentration for OPAR and pOPAR is plotted in Figure 5.7. Both OPAR and pOPAR decrease the growth rate of HA crystals. At concentrations up to 2 μg/ml the two peptides have approximately the same effect in reducing the growth rate, but the growth rate in the presence of pOPAR is consistently slightly lower. This result again suggests that the 11 aspartic acid residues in the two peptides prevent HA crystals from growing and that the additional phosphate in pOPAR increases its inhibition potency.

The role of phosphate groups in the interaction between OPN-related peptides and biominerals has been studied using molecular dynamics (MD) simulations. These simulations have investigated the interaction of peptides with the surface of hydroxyapatite [39] as well as with calcium oxalate monohydrate (COM, $CaC_2O_4.H_2O$) which is also found in kidney stones [30]. The OPN-related peptides we studied are negatively charged and are attracted to the Ca^{2+}-rich {100} faces of HA and COM. More potent inhibitors are attracted more closely to the {100} faces of both HA and COM [30,39]. The simulations of Azzopardi et al. [39] and Grohe et al.

[30] suggested that the adsorption of acidic peptides to the {100} face of these biominerals is governed by electrostatics and is not dependent on the particular amino-acid sequence.

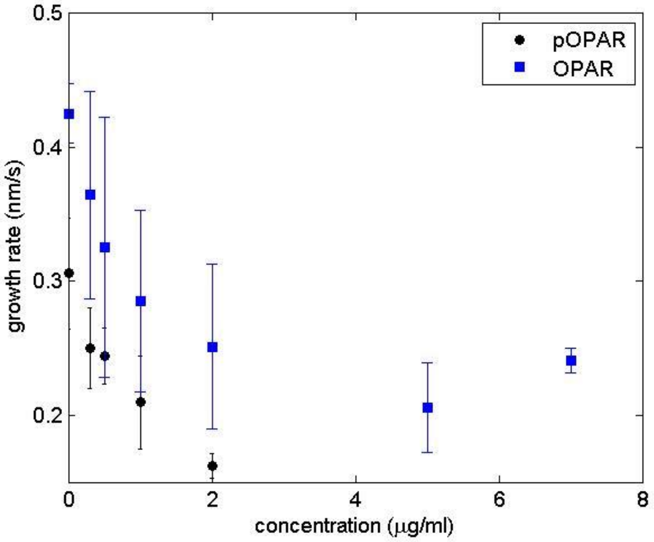

Figure 5. 7: Growth rate as a function of concentration for OPAR and pOPAR P3 at $\bar{r}_h = 20\ 0nm$.

The analysis of Azzopardi et al. suggested that the adsorption strength is inversely related to the isoelectric point, PI, of the peptide. The PI is the *p*H value at which the molecule carries no net electrical charge. Azzopardi et al. found in their simulations that the peptides which approached the {100} face of HA closely were those with the lowest PI. In other words, more inhibitory peptides have lower isoelectric points than less inhibitory peptides. They calculated PI for four virtual peptides: OPAR, pOPAR, P0, and P3, which is shown in Table 5.1.

Azzopardi's simulations showed that pOPAR, which includes the poly aspartic acid sequence of OPN, formed the closest contact with the {100} face of HA. In addition to the aspartic acids, the single phosphoserine approached the {100} face most closely.

Atomic scale molecular dynamics simulations performed by Grohe et al. found that the triply-phosphorylated peptide P3, absorbed to the {100} crystal face of COM much more rapidly than the singly-phosphorylated P1. They concluded that the phosphates on the phosphoserines drove the peptide close to the COM crystal face, leading to the more effective inhibition of crystal growth. Of interest, the authors noted that the acidic amino acid residues in P3 were found closer to the crystal face than the phosphates.

The inhibition of HA growth by pOPAR, OPAR, P3 and P0 has also been studied by the constant composition seeded growth method by Azzopardi et al. [39]. Based on the effects of these peptides on the seeded growth of HA, they determined the concentration of a particular peptide needed to inhibit the crystal growth by half. This is referred to as the IC_{50} value. A larger IC_{50} value is indicative of less inhibitory strength. Their results are summarized in Table 5.1 [39].

The work of Azzopardi et al. and Grohe et al. indicated that P0 has weak inhibitory activity. Our results on P0 are in good agreement with theirs [30,39]. Table 5.1 compares our DLS results with those of Azzopardi et al. Based on the DLS results, the order of the inhibitory effect on HA growth at 2 μg/ml peptide concentrations is pOPAR>OPAR>P3>P0. Measurements were not done on P0 at 2 μg/ml, but based on data at higher concentration its inhibitory effect is expected to be less than that of P3. Grohe's simulations established the order of inhibitory potency on COM crystals for the OPN-derived peptides that they studied to be P3>P1>P0.

Table 5.1 indicates a small difference in the PI values of OPAR and pOPAR, which implies that both have similar inhibitory potency due to the presence of the aspartic acid residues. Our DLS results confirm that inhibitory potency increased with the addition of one phosphate group. We showed that OPAR prevents HA formation, while phosphorylation of OPAR in addition to inhibiting the nucleation of HA causes a decrease in crystal growth. This explanation is also true for P3. Having three extra phosphates enhanced the inhibitory potency of P3 over that of P0. Based on the constant composition (CC) seeded HA growth, IC_{50} value, and the calculated PI value, the order of inhibitory potency for the OPN-derived peptides to be P3>pOPAR>OPAR>P0. Although the position of P3 in this sequence is different in our results from in those of Azzopardi et al., both studies show that phosphorylations play a key role in inhibition potency of peptides.

Table 5. 1: Inhibitory potency of OPN peptides, adopted from [39] and DLS results.

Peptide	PI value	IC_{50} (μg/ml) (CC)	Growth rate (nm/s) for 2 μg/ml inhibitors (DLS)	Mean normalized hydrodynamic radius (nm) for 2 μg/ml inhibitors (DLS)
P3	2.92	1.48	0.200	0.910
pOPAR	3.39	1.93	0.180	0.840
OPAR	3.60	2.97	0.186	0.870
P0	4.17	>75	0.308 (at 5 μg/ml)	1.029 (at 5 μg/ml)

The DLS and the constant-composition experiments are different, so it is difficult to compare them directly. In the DLS experiment, the composition of the solution varies as new crystals nucleate and grow, while in the constant-composition experiment the composition of the solution is kept fixed as pre-existing seed crystals grow. Although the constant-composition assay is not able to investigate nucleation or the early stages of crystal growth, the work of Azzopardi et al. indicates the inhibiting potency is more pronounced for the phosphorylated peptides, which is fully consistent with our DLS results.

5.3 Bone sialoportein

Based on previous observations [20,47], it was postulated that BSP would cause the spontaneous nucleation of crystals below the normal threshold concentrations of calcium and phosphate ions. We therefore studied the effect of adding rBSP to solutions with different concentrations of calcium and phosphate ions.

First we tried to find a concentration of calcium and phosphate ions at which precipitation of crystals does not happen in the absence of rBSP, but did happen in the presence of rBSP. A solution of 5.20 mM Ca^{2+} and 3.25 mM PO_4^{3-} was chosen. Since in this case the scattered light intensity is very low, the data are noisy. The count rate is quite small but did increase slightly over time, indicating that some crystals precipitated. Therefore, if indeed there is a threshold for the precipitation of particles, the chosen ion concentrations are still slightly above it. The second solution contained higher calcium and phosphate ion concentrations, 5.40 mM Ca^{2+} and 3.37 mM PO_4^{3-}, and significant precipitation did occur in the absence of rBSP.

For the first case, our DLS results suggested that rBSP may enhance nucleation at very low concentrations, but appears to inhibit growth at concentrations higher than 2 μg/ml.

For the second solution, the results show a delay in the increase of $\bar{r}_h$ for protein concentrations exceeding 1 μg/ml. Unlike the case of lower ion concentration, here the presence of rBSP delays the nucleation of the particles, and the delay time becomes larger as the concentration increases. The observed behaviour of rBSP in the solution with higher ion concentrations is similar to that observed for OPN in this work, and for p-rOPN in [75]. However, this inhibitory effect is less significant than that observed with OPN. Furthermore, our data at the higher ion concentrations suggest that there are more small particles in the presence of the protein than in the control experiment, suggesting that rBSP promotes the nucleation of HA crystals. It is of interest that with both rBSP and nOPN, the growth rate of the HA crystals is enhanced. It is postulated that since BSP and OPN have a high affinity for HA crystals, they will gradually be removed from the solution as the crystals form. Once this happens, the few crystals can grow at a faster rate than that seen in control solutions because of the increased availability of calcium and phosphate ions to drive growth [75].

Previous studies [20,47] have shown that BSP nucleates HA formation in agarose gel and solid-phase collagen. Nucleation of HA precipitation by BSP was first observed in steady-state agarose gel experiments in 1993 [20]. Hunter and Goldberg observed the formation of HA in a gel containing BSP under conditions of sub-threshold calcium and phosphate saturation. Their studies suggested that the glutamic acid-rich sequences of BSP played a key role in the nucleation of HA crystals [20]. The chemical nature of the BSP-collagen interaction was investigated by Baht et al. in 2008 [47]. It was found that hydrophobic interactions were responsible for the binding of BSP to collagen and, based on previous studies [61], electrostatic forces appear to stabilize the interaction. In contrast, other proteins, such as dentin phosphophoryn and dentin matrix protein-1, bind to collagen electrostatically [47]. The acidic amino-acid-rich regions of these proteins are involved in collagen binding. It has been shown that the nucleation potency of BSP increases 10-fold when it is incubated in collagen as compared to agarose [47].

Hunter et al. in 1996 reported that in solution studies, BSP at concentrations up to 10 μg/ml had no effect on hydroxyapatite formation [22]. BSP and its peptides were shown to have an inhibitory effect of on crystal growth by Stubbs et al. [68]. In their system, which used a seeded HA crystal assay, native BSP and one of its major fragments were able to suppress crystal growth. They found that recombinant BSP could also block the growth of HA seeded crystals suspended in supersaturated solution of calcium and phosphate, but was not as potent as the native protein. This suggests that post translational modifications contribute to the ability of BSP to inhibit crystal growth [68].

Goldberg et al. in 1996 suggested that although PTMs are not necessary for nucleation of BSP, lack of these modifications decrease the potency of the protein [58]. Tye et al. in 2003 compared the nucleating activity of nBSP and rBSP. Their results were in good agreement with those of Goldberg et al., and showed that the nucleation activity of BSP resides in two glutamic acid domains [50].

Molecular dynamics simulations on BSP-derived peptides suggest that the particular sequence of amino acids is not the only factor that determines the nucleation potency of the peptide, but that the peptide structure is also important [65].

The effect of dentin phosphophoryn (DPP) on hydroxyapatite formation and growth has been studied in an *in vitro* gelatin gel diffusion system [85]. At high concentrations of DPP (100 μg/ml), the *de novo* formation of HA decreases, while low concentrations of protein (0.010-1 μg/ml) promoted *de novo* hydroxyapatite formation. These data suggest that DPP has a multifunctional role in the mineralization process [85]. DPP attached to agarose beads or collagen has also been shown to promote HA formation [86-89]. Thus it appears the formation of HA is promoted by immobilized DPP and hindered by high concentrations of DPP in solution. This appears to be similar to the behavior we observed for BSP, although more experimental work is needed to confirm this.

Our results in general agree with the previously published studies on BSP and HA formation, although nucleation potency was not readily apparent by DLS. Additional effort is required to develop the most appropriate protocol for studying mineral nucleation. However, it is also possible that BSP does not nucleate well or at all in solution. The previously published studies showing BSP-mediated nucleation of hydroxyapatite were done in steady-state agarose or collagen-gel systems, suggesting that confinement or constraints on the protein conformation may play a role.

There is good evidence in the literature to support BSP-mediated inhibition of crystal growth. Our results are also in general agreement with this. Overall, the scattered intensity due to precipitating calcium phosphate is decreased by the addition of BSP, and while some crystals do become large, it appears that the majority do not. It would be of interest to determine if further addition of BSP, for example 20 minutes into a run, would affect the growth of these crystals.

Overall, it seems that the behaviour of BSP is more complicated than the other proteins. We did not observe unambiguous nucleation under the experimental conditions we investigated. However there do seem to be similarities between our observations for BSP and what others have seen for DPP [85]. Many questions remain and substantial additional studies are needed to clarify the behaviour of BSP.

Chapter 6: Conclusions and Future Work

6.1 Conclusions

Improved understanding of the effect of modulatory proteins on the crystallization of hydroxyapatite could eventually lead to the development of drugs or bone repair therapies to control pathological calcifications resulting from the breakdown of the body's natural biomineralization regulatory system.

Dynamic light scattering has proven to be a versatile and convenient method to monitor the formation process of HA. DLS data provide information about the size distribution of the HA crystals and their concentrations in aqueous solutions that is not available from other techniques. This technique allows us to distinguish the effects of proteins and peptides on nucleation and growth separately. DLS provides an alternative approach to constant composition and steady state assays for examining the effects of bone-related proteins or synthetic peptides on the *in vitro* formation of HA.

We used DLS to measure the time evolution of the particle size distribution and average scattered light intensity of HA crystals in the presence of proteins and peptides at particular ionic concentration and *p*H conditions.

We found that native OPN inhibits the nucleation of HA crystals, while the non-phosphorylated rOPN strongly inhibits their growth. This confirms that phosphorylation of OPN is critical for the inhibition of nucleation, while the acidic amino acid groups alone can inhibit crystal growth.

We also studied the inhibitory effects of some synthetic OPN-related peptides. Our results show that P0 exhibits a very weak inhibitory effect on the growth of HA crystals, while P3, with three phosphate groups added to the same amino acid sequence, is a potent inhibitor of HA nucleation. The peptide OPAR is found to moderately inhibit nucleation. On the other hand, the phosphorylated version of OPAR not only reduced the number of calcium-phosphate particles but also slightly slowed their growth. Overall, we found the order of inhibitory potency of the four OPN-derived peptides to be pOPAR>OPAR>P3>P0.

Our results for rBSP showed that for sub-threshold concentrations of calcium and phosphate it appears to function as a nucleator at lower protein concentrations, and very likely as an inhibitor of crystal growth at higher concentrations of protein.

6.2 Future Work

We tried to investigate the nucleation potency of BSP using DLS, but had little success. Additional effort is required to find the appropriate working concentrations of calcium and phosphate for studying the nucleation process and the question of whether BSP enhances mineralization from a solution. Additional study is also needed to determine whether the action of BSP is different in solution than it is in a gel, and if so, to understand the reasons for the difference.

Since acidic proteins become nucleators of HA when immobilized, it would be intriguing to attempt DLS experiments using BSP and OPN covalently linked to agarose beads.

If a protocol for a DLS-based nucleation assay can be established, DLS could be used to investigate the effects of BSP-derived peptides, the roles of PTMs in BSP, the effects of altering the poly-Glu sequences of BSP, and the effects of other protein modulators of biominerals.

Our investigations have shown that several proteins and peptides are effective in inhibiting HA nucleation or growth. It would be of interest to analyze the effect of mixtures of different inhibitors using DLS.

It would be useful to characterize the morphology of the crystal structures and precipitant at different stages of growth using XRD. Stopping crystal formation at early times and analyzing the crystals with XRD would provide insight in to the nature of the precipitating particles and the process by which HA crystals form in these solutions [70].

All of our DLS experiments to date have been performed at room temperature. Since the solubility of the calcium phosphate decreases as the temperature is lowered, performing DLS experiments at physiological temperature would be a good idea. In addition, experiments as a function of temperature may provide an alternate way to investigate nucleation and inhibition.

References

[1] Bengtson S., Palaeontology: A ghost with a bite. Nature 2006, 442, 146-147.

[2] Lowenstam H.A., Minerals formed by organisms. Science 1981, 211, 1126-1131.

[3] Addadi L., Joester D., Nudelman F., Weiner S., Mollusk shell formation: a source of new concepts for understanding biomineralization processes. Chemistry 2006, 12, 980-987.

[4] Mann S., Biomineralization: Principles and concepts in bioinorganic materials chemistry. New York, Oxford University Press, 2001.

[5] Azzopardi P.V., Inhibition of Hydroxyapatite growth by osteopontin phosphopeptides. M.Sc. Thesis, Western University, 2009.

[6] Franceschi V.R., Horner H.T., Calcium oxalate crystals in plants. Bot. Rev. 1980, 46, 361-427.

[7] Webb M. A., Cell-mediated crystallization of calcium oxalate in plants. Plant Cell 1999, 11, 751-761.

[8] Weiner S., Dove P.M., An overview of biomineralization processes and the problem of the vital effect. Rev. Mineral. Geochem. 2003, 54, 1-29.

[9] Schlieper G, Westenfeld R, Brandenburg V, Ketteler M, Inhibitors of calcification in blood and urine. Semin. Dial. 2007, 20, 113-121.

[10] Giachelli C.M, Ectopic calcification: gathering hard facts about soft tissue mineralization. Am. J. Pathol. 1999, 154, 671–675.

[11] Cohen M.M.Jr., The new bone biology: pathologic, molecular, and clinical correlates. Am. J. Med. Genet. A 2006, 140, 2646-2706.

[12] Baht G.S., Effect of collagen-binding and phosphorylation in BSP-mediated hydroxyapatite nucleation. Ph.D. Thesis, Western University, 2009.

[13] Dorozhkin SV, Epple M., Biological and medical significance of calcium phosphates. Angew. Chem. Int. Ed. Engl. 2002, 41, 3130-3146.

[14] De Yoreo J.J., Vekilov P.G., Principles of crystal nucleation and growth. Rev. Mineral. Geochem. 2003, 54, 57-93.

[15] Mann S., Mineralization in biological systems. Struct. Bonding. 1983, 54, 125-174.

[16] Cuisinier F.J.G., Steuer P., Brisson A., Voegel J.C., High resolution electron microscopy study of crystal growth mechanisms in chicken bone composites. J. Cryst. Growth 1995, 156, 443-453.

[17] Cuisinier F.J.G., Bone mineralization. Curr. Opin. Solid State Mater. Sci. 1996, 1, 436-439.

[18] George A., Veis A., Phosphorylated proteins and control over apatite nucleation, crystal growth, and inhibition. Chem.Rev. 2008, 108, 4670-4693.

[19] Goldberg H.A., Hunter G.K., The inhibitory activity of osteopontin on hydroxyapatite formation in vitro. Ann. NY Acad. Sci. 1995, 760, 305-308.

[20] Hunter G.K., Goldberg H.A., Nucleation of hydroxyapatite by bone sialoprotein. Proc. of the Nat. Acad. of Sci. 1993, 90, 8562-8565.

[21] Boden S.D., The ABC's of BMP's. Orthop. Nurs. 2005, 24, 49-52.

[22] Hunter G.K., Hauschka P.V., Poole A.R., Rosenberg L.C., Goldberg H.A., Nucleation and inhibition of hydroxyapatite formation by mineralized tissue proteins. Biochem. J. 1996, 317 (pt1), 59-64.

[23] Boskey A.L., Maresca M., Ullrich W., Doty S.B., Butler W.T., Prince C.W., Osteopontin-hydroxyapatite interactions in-vitro: inhibition of hydroxyapatite formation and growth in a gelatin gel. Bone Miner. 1993, 22, 147-159.

[24] Pampena, D.A., Robertson K.A., Litvinova O., Lajoie G., Goldberg H.A., Hunter G.K., Inhibition of hydroxyapatite formation by osteopontin phosphopeptides. Biochem. J. 2004, 378 (Pt3), 1083-1087.

[25] Jono S., Peinado C., Giachelli C.M., Phosphorylation of osteopontin is required for inhibition of vascular smooth muscle cell calcification. J. Biol. Chem. 2000, 275, 20197-20203.

[26] Luo G., McKee M.D., Pinero G.J., Loyer E., Behringer R.R., Karsenty G., Spontaneous calcification of arteries and cartilage in mice lacking matrix GLA protein. Nature 1997, 386, 78-81.

[27] Goiko M., Dierolf J., Gleberzon J.S., Liao Y., Grohe B., Goldberg H.A., de Bruyn J.R., Hunter G.K., Peptides of Matrix Gla protein inhibit nucleation and growth of hydroxyapatite and calcium oxalate monohydrate crystals. submitted to PLoS One.

[28] Goiko M., dynamic-light-scattering-based characterization of the inhibitory effects of matrix gla protein peptides on hydroxyapatite nucleation and growth. B.Sc. Thesis, Western University, 2012.

[29] Keykhosravani M., Doherty-Kirby A., Zhang C., Brewer D., Goldberg H.A., Hunter G.K., Lajoie G., Comprehensive identification of post-translational modifications of rat bone osteopontin by mass spectrometry. Biochem. J. 2005, 44, 6990-7003.

[30] Grohe B., O'Young J., Ionescu D.A., Lajoie G., Rogers K.A., Karttunen M., Goldberg H.A., Hunter G.K., Control of calcium oxalate crystal growth by face-specific adsorption of an osteopontin phosphopeptide. J. Amer. Chem. Soc. 2007, 129, 14946-14951.

[31] Rangaswami H., Bulbule A., Kundu G.C., Osteopontin: role in cell signaling and cancer progression. Trends Cell Biol. 2006, 16, 79-87.

[32] Grohe B., Taller A., Vincent P.L., Tieu L.D., Rogers K.A., Heiss A., Sørensen E.S., Mittler S., Goldberg H.A., Hunter G.K., Crystallization of calcium oxalates is controlled by molecular hydrophilicity and specific polyanion-crystal interactions. Langmuir 2009, 25, 11635-11646.

[33] Giachelli C.M., Inducers and inhibitors of biomineralization: lessons from pathological calcification. Orthod. Craniofac. Res. 2005, 8, 229-231.

[34] Giachelli C.M., Steitz S., Osteopontin: a versatile regulator of inflammation and biomineralization. Matrix Biol. 2000, 19, 615-622.

[35] Mazzali M., Kipari T., Ophascharoensuk V., Wesson J. A., Johnson R., Hughes J., Osteopontin a molecule for all seasons. Quarterly J. Med. 2002, 95, 3-13.

[36] http://www.ncbi.nlm.nih.gov/protein/P08721.2, Gene ID= 25353.

[37] Hincke M.T., St. Maurice M., Phosphorylation-dependent modulation of calcium carbonate precipitation by chicken eggshell matrix proteins. In: Goldberg M., Boskey A., Robinson C., editors. Chemistry and biology of mineralized tissues, Rosemount: Am. Acad. Orthop. Surg. 2000, 13-17.

[38] Hunter G.K., Kyle C.L., Goldberg H.A., Modulation of crystal formation by bone phosphoproteins: structural specificity of the osteopontin-mediated inhibition of hydroxyapatite formation. Biochem. J. 1994, 300, 723-728.

[39] Azzopardi P.V., O'Young J., Lajoie G., Karttunen M., Goldberg H.A., Hunter G.K., Roles of electrostatics and conformation in protein-crystal interactions. PLoS One 2010, 5, e9330 1-11.

[40] Dauphinee R., Effect of osteopontin and related peptides on hydroxyapatite crystallization studied by dynamic light scattering. M.Sc. Thesis, Western University, 2009.

[41] Shiraga H., Min W., Van Dusen W.J., Clayman M.D., Miner D., Terrell C.H., Sherbotie J.R., Foreman J.W., Przysiecki C., Neilson E.G., Inhibition of calcium oxalate crystal growth in

vitro by uropontin: Another member of the aspartic acid-rich protein superfamily. Proc. Nat. Acad. Sci. USA 1992, 89, 426-430.

[42] Hoyer J.R., Asplin J.R., Otvos L., Phosphorylated osteopontin peptides suppress crystallization by inhibiting the growth of calcium oxalate crystals. Kidney Int. 2001, 60, 77-82.

[43] Oldberg, A., Franzen, A., Heinegard, D., Cloning and sequence analysis of rat bone sialoprotein (osteopontin) cDNA reveals an Arg-Gly- Asp cell binding sequence. Proc. Nat. Acad. Sci. USA 1986, 83, 8819-8823.

[44] Ito S., Saito T., Amano K., In vitro apatite induction by osteopontin: interfacial energy for hydroxyapatite nucleation on osteopontin. J. Biomed. Mater. Res. A. 2004, 69, 11-16.

[45] Gericke A., Qin C., Spevak L., Fujimoto Y., Butler W.T., Sørensen E.S., Boskey A.L., Importance of phosphorylation for osteopontin regulation of biomineralization. Calcif. Tissue Int. 2005, 77, 45-54.

[46] Wang L., Guan X., Tang R., Hoyer J.R., Wierzbicki A., De Yoreo J.J., Nancollas G.H., Phosphorylation of osteopontin is required for inhibition of calcium oxalate crystallization. J. Phys. Chem. B. 2008, 112, 9151-9157.

[47] Baht S.G., Hunter G.K., Goldberg A.H., Bone sialoprotein–collagen interaction promotes hydroxyapatite nucleation. Matrix Biol. 2008, 27, 600-608.

[48] Goldberg H.A., Warner K.J., Li M.C., Hunter G.K., Binding of bone sialoprotein, osteopontin and synthetic polypeptides to hydroxyapatite, Connect. Tissue Res. 2001, 42, 25–37.

[49] Fisher L.W., McBride O.W., Termine J.D., Young M.F., Human bone sialoprotein. Deduced protein sequence and chromosomal localization. J. Biol. Chem. 1990, 265, 2347-2351.

[50] Tye C.E., Rattray, K.R. Warner K.J., Gordon J.A., Sodek J., Hunter G.K., Goldberg H.A., Delineation of the hydroxyapatite-nucleating domains of bone sialoprotein. J. Biol. Chem. 2003, 278, 7949-7955.

[51] Ganss B., Kim R.H., Sodek J., Bone sialoprotein. Crit. Rev. Oral Biol. Med. 1999, 10, 79-98.

[52] Franzen A., Heinegard D., Isolation and characterization of two sialoproteins present only in bone. Biochem. J. 1985, 1 232, 715-724.

[53] Carlinfante G., Vassiliou D., Svensson O., Wendel M., Heinegård D., Andersson G., Differential expression of osteopontin and bone sialoprotein in bone metastasis of breast and prostate carcinoma. Clin. Exp. Metastasis 2003, 20, 437-444.

[54] Waltregny D., Bellahcène A., Van Riet I., Fisher L.W., Young M., Fernandez P., Dewé W., de Leval J., Castronovo V., Prognostic value of bone sialoprotein expression in clinically localized human prostate cancer. J. Natl. Cancer Inst. 1998, 90, 1000-1008.

[55] Bellahcene A., Maloujahmoum N., Fisher L.W., Pastorino H., Tagliabue E., Ménard S., Castronovo V. , Expression of bone sialoprotein in human lung cancer. Calcif. Tissue Int. 1997, 61, 183-188.

[56] Bellahcene A., Albert V., Pollina L., Basolo F., Fisher L.W., Castronovo V., Ectopic expression of bone sialoprotein in human thyroid cancer. Thyroid 1998, 8, 637-641.

[57] Oldberg A., Franzen A., Heinegard D., The primary structure of a cell-binding bone sialoprotein. J. Biol. Chem. 1988, 263, 19430–19432.

[58] Goldberg H A., Warner K.J., Stillman M.J., Hunter G.K., Determination of the hydroxyapatite-nucleating region of bone sialoprotein. Connect. Tissue Res. 1996, 35, 385-392.

[59] Fisher L.W., Torchia D.A., Fohr B., Young M.F., Fedarko N.S., Flexible structures of SIBLING proteins, bone sialoprotein, and osteopontin. Biochem. Biophys. Res. Comun. 2001, 280, 460-465.

[60] Wuttke M., Muller S., Nitsche D.P., Paulsson M., Hanisch F.G., Maurer P., Structural characterization of human recombinant and bone-derived bone sialoprotein. Functional implications for cell attachment and hydroxyapatite binding. Biochem. J. 2001, 276, 36839-36848.

[61] Tye C.E., Hunter G.K., Goldberg H.A., Identification of the type I collagen-binding domain of bone sialoprotein and characterization of the mechanism of interaction. J. Biol. Chem. 2005, 280, 13487-13492.

[62] Karadag A., Ogbureke K.U., Fedarko N.S., Fisher L.W., Bone sialoprotein, matrix metalloproteinase 2, and alpha(v)beta3 integrin in osteotropic cancer cell invasion. J. Natl. Cancer Inst. 2004, 96, 956–965.

[63] Fedarko N.S., Fohr B., Robey P.G., Young M.F., Fisher L.W., Factor H binding to bone sialoprotein and osteopontin enables tumor cell evasion of complement-mediated attack. J. Biol. Chem. 2000, 275, 16666–16672.

[64] Gordon J., Sampaio A., Underhill T.M., Hunter G.K., Goldberg H.A., Bone sialoprotein expression affects osteoblast differentiation and matrix mineralization in vitro. Bone 2007, 41, 462-473.

[65] Baht G.S., O’Young J., Borovina A., Chen H., Tye C.E., Karttunen M., Lajoie G.A., Hunter G.K., Goldberg H.A., Phosphorylation of Ser136 is critical for potent bone sialoprotein-mediated nucleation of hydroxyapatite crystals. Biochem. J. 2010, 428, 385-395.

[66] Yang Y., Cui Q., Sahai N., How does bone sialoprotein promote the nucleation of hydroxyapatite? A molecular dynamics study using model peptides of different conformations. Langmuir 2010, 26, 9848-9859.

[67] Malaval L., Wade-Guéye N.M., Boudiffa M., Fei J., Zirngibl R., Chen F., Laroche N., Roux J.P., Burt-Pichat B., Bone sialoprotein plays a functional role in bone formation and osteoclastogenesis. J. Exp. Med. 2008, 205, 1145-1153.

[68] Stubbs J.T, Mintz K.P., Eanes E.D., Torchia D.A., Fisher L.W., Characterization of native and recombinant bone sialoprotein: delineation of the mineral-binding and cell adhesion domains and structural analysis of the RGD domain. J. Bone Min. Res. 1997, 12, 1210-1222.

[69] Banerjee S., Tyagi A.K., Functional materials: preparation, processing and applications. Burlington, Elsevier Science, 2011.

[70] Onuma K., Ito A., Cluster growth model for hydroxyapatite. Chem. Mater. 1998, 10, 3346-3351.

[71] Oyane A., Onuma K., Kokubo T., Ito A., Clustering of calcium phosphate in the system CaCl2-H3PO4-KCl-H2O. J. Phys. Chem. B. 1999, 103, 8230-8235.

[72] Onuma K., Oyane A., Tsutsui K., Tanaka K., Treboux G., Kanzaki N., Ito A., Precipitation kinetics of hydroxyapatite revealed by the continuous-angle laser light-scattering technique. J. Phys. Chem. B. 2000, 104, 10563-10568.

[73] Onuma K., Kanzaki N., Kobayashi N., Association of calcium phosphate and broblast growth factor-2: a dynamic light scattering study. Macromol. Biosc. 2004, 4, 39-46.

[74] Kamiya N., Tsunomori F., Kagi H,, Notsu K., Dynamic light scattering study of the inhibiting effect on crystal growth of calcium carbonate. Bull. Chem. Soc. Jpn. 201, 84, 344-348.

[75] de Bruyn J.R., Goiko M., Mozaffari M., Bator D., Dauphinee R.L., Liao Y., Flemming R.L., Bramble M.S., Hunter G.K., Goldberg H.A., Dynamic light scattering study of inhibition of nucleation and growth of hydroxyapatite crystals by osteopontin. PLoS One 2013, 8, e56764.

[76] Berne B.J., Pecora R. Dynamic Light Scattering with applications to chemistry, biology and physics. New York, Dover Publications, 2000.

[77] Frisken B.J., Revisiting the method of cumulants for the analysis of dynamic light-scattering data. Appl. Opt. 2001, 40, 4087-4091.

[78] Lucius A.L., Veronese P.K., Stafford R.P., Dynamic light scattering to study allosteric regulation. Methods Mol. Biol. 2012, 796, 175-186.

[79] Onuma K., Recent research on pseudobiological hydroxyapatite crystal growth and phase transition mechanisms. Prog. Cryst. Growth Charact. Mat. 2006, 52, 223-245.

[80] Ruso J., Pinerio A., Proteins in solution and interfaces: methods and applications in biotechnology and materials science. New Jersey, Wiley, 2013

[81] Hughes, Andrew B., Amino acids, peptides and proteins in organic chemistry, analysis and function amino acids and peptides. New Jersey, Wiley, 2013.

[82] Zhang Q., Domenicucci C., Wrana J.L., Sodek J., Characterization of fetal porcine bone sialoproteins, secreted phosphoprotein I (SPPI, osteopontin), bone sialoprotein, and a 23 kDa glycoprotein. Demonstration that the 23 kDa glycoprotein is derived from the carboxyl terminus of SPPI. J. Biol. Chem. 1990, 265, 7583-7589.

[83] Dyuzheva M.S., Kargu O.V., Klyubin V.V., The effect of polydispersity on the size of colloidal particles determined by the dynamic light scattering. Colloid J. 2002, 64, 39-45.

[84] Hunter G.K., Goldberg H.A., Modulation of crystal formation by bone phosphoproteins: role of glutamic acid-rich sequences in the nucleation of hydroxyapatite by bone sialoprotein. Biochem. J. 1994, 302 (Pt 1), 175-179.

[85] Boskey A.L., Maresca M., Doty S., Sabsay B., Veis A., Concentration-dependent effects of dentin phosphophoryn in the regulation of in vitro hydroxyapatite formation and growth. Bone Mine. 1990, 11, 55-65.

[86] Lussi A., Crenshaw M.A., Linde A., Induction and inhibition of hydroxyapatite formation by rat dentine phosphoprotein in vitro. Arch. Oral Biol.1988, 33, 685-691.

[87] Linde A., Lussi A., Crenshaw M.A., Mineral induction by immobilized polyanionic proteins. Calcif. Tissue Int. 1989, 44, 286-295.

[88] Doi Y., Horiguchi T., Kim S.H., Morikawa Y., Wakamatsu N., Adachi M., Shigeta H., Sasaki S., Shimokawa H., Immobilized DPP and other proteins modify OCP formation. Calcif. Tissue Int. 1993, 52, 139-145.

[89] Van den Bos T., Steinfort J., Beertsen W., Effect of bound phosphoproteins and other organic phosphates on alkaline phosphatase-induced mineralization of collagenous matrices in vitro. Bone Mine. 1993, 23, 81-93.

[90] Flemming RL, Micro X-ray Diffraction (mXRD): A versatile technique for characterization of Earth and planetary materials. Can. J. Earth Sci. 2007, 44, 1333-1346.

[91] Manske M., The chemistry of proteins 2005. Wikimedia Laboratories: en.labs.wikimedia.org/wiki/Biochemistry/Proteins/The_chemistry_of_proteins.

Appendix

The twenty essential amino acids. The residues are shown in uncharged state. The three-letter and one-letter abbreviations are given below the chemical structure of each amino acid [91].

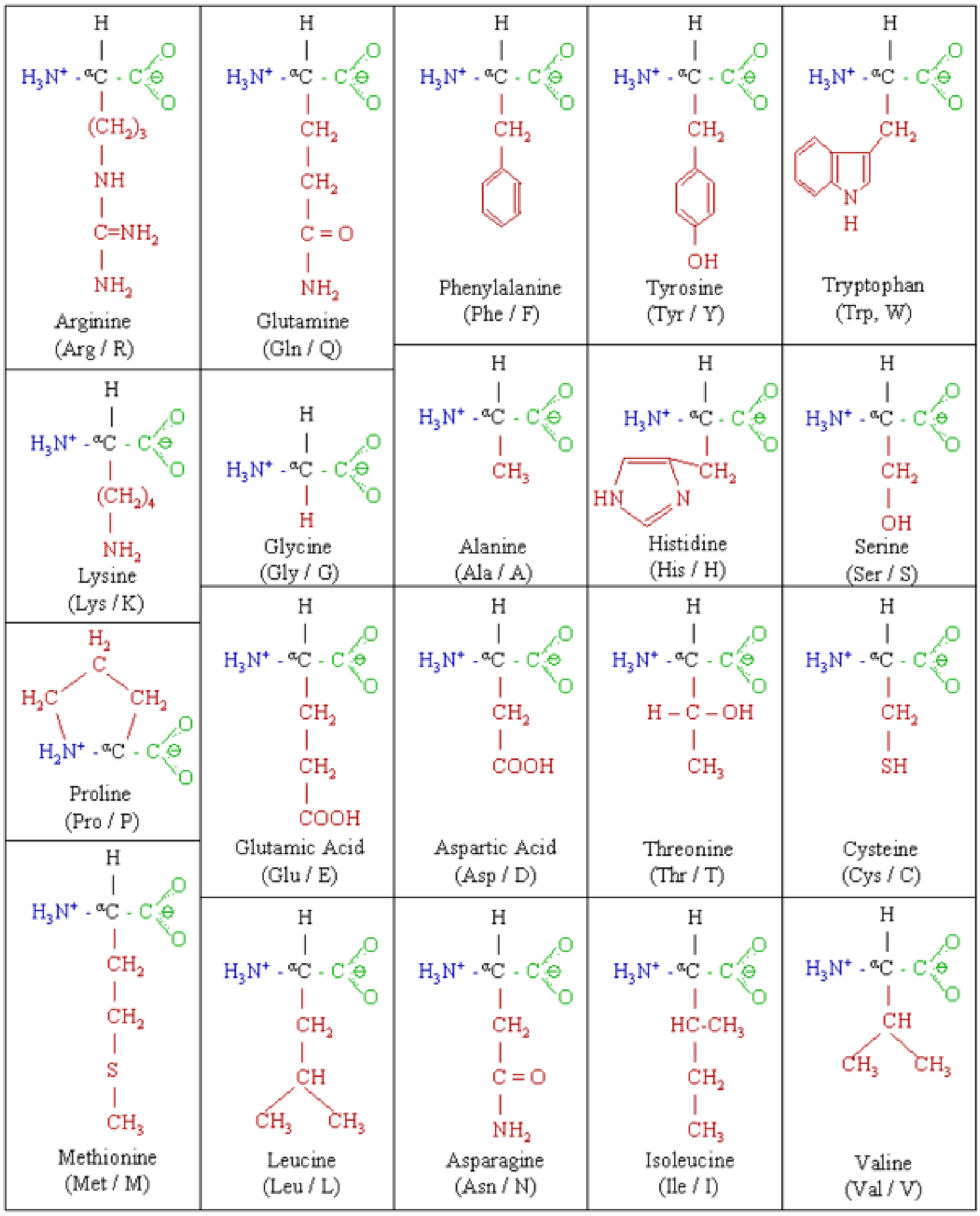

Curriculum Vitae

Name:	Maryam Mozaffari
Post-secondary Education and Degrees:	Islamic Azad University Tehran, Iran 2000-2004 B.Sc.
	Islamic Azad University Tehran, Iran 2005-2008 M.Sc.
	The University of Western Ontario London, Ontario, Canada 2011-2013 M.Sc.
Related Work Experience	Research and Teaching Assistant The University of Western Ontario 2011-2013

Publications:

- **Journal Articles:**
  1. J. de Bruyn, M. Goiko, **M. Mozaffari**, D. Bator, R. Dauphinee, Y. Liao, R. Fleming, G. Hunter, H. Goldberg *"Dynamic light scattering study of inhibition of nucleation and growth of hydroxyapatite"*, PLOS ONE 2013, 8, e56764.
  2. R. Malekfar, A. M. Nikbakht, S. Abbasian, F. Sadeghi, **M. Mozaffari**, *"Evaluation of tomato juice quality using Surface Enhanced Raman Spectroscopy (SERS)"*, Acta Physica Polonica A 117 (2010) 333-335.

- **Conference Presentations:**

  1. S. Abbasian, F. Sadeghi, R. Malekfar, M. Khosro, **M. Mozafari**, *"Synthesis, Characterization and Experimental Investigation of Surface Activity of Three Different SERS Substrates"*, Proceedings of the 10th Conference on Condensed Matter Physics, Physics Society of Iran, Jan. 26-27 2011, University of Shiraz, Shiraz, Iran.
  2. **M. Mozaffari**, R. Malekfar, S. Abbasian, *"TiO_2 Rutile Phase Active Modes Investigation at Low Temperatures down to 10K"*, Proceedings of the 16th Annual IASBS Meeting on Condensed Matter Physics, May. 27-28 2010, Institute for Advanced Studies in Basic Science, Gava Zang, Iran.
  3. R. Malekfar, N. Mohammadian, **M. Mozaffari**, *"The effect of High DC Electric Field on the Intensities of Raman Active Modes of Anatase TiO_2 Nanoparticles"*, Proceedings of the 2nd International Congress on Nanoscience & Nanotechnology (ICNN2008), Oct. 28-30 2008, University of Tabriz, Tabriz, Iran.
  4. **M. Mozaffari**, R. Malekfar, *"Raman study of Anatase TiO_2 Nanoparticles at Low Temperatures"*, Proceedings of the 4th Nanotechnology Student Conference, Oct. 8-10 2008, Razi University, Kermanshah, Iran.
  5. A. Shirpaei, R. Malekfar, Y. Ghasemian, **M. Mozaffari**, *"Anatase TiO_2 Nanoparticles Phase Change Investigation at High Temperatures by Back Scattering Raman Spectroscopy"*, Proceedings of the 17th European

Conference on Dynamics of Molecular Systems (MOLEC2008), Aug. 23-28 2008, St. Petersburg, Russia.

6. R. Malekfar, **M. Mozaffari**, S. Mihanyar, *"Phase Changes Investigation of Nanostructured* TiO_2 *by Back Scattering Dispersive Micro Raman Spectroscopy"*, Proceedings of 12th Annual Iranian conference of Physics, Aug. 27-30 2007, Yasouj University, Kohgiloye and Bouyer-ahmad, Iran.
7. R. Malekfar, S. Mihanyar, **M. Mozaffari**, *"The micro-Raman scattering spectroscopy investigation of nano-crystalline phases of* TiO_2 *powder by Sol-Gel method"*, Proceedings of 1st Sharjah International Conference on Nanotechnology and its Applications (AIP conference proceedings, Vol. 929, 167-171), Apr. 10-12 2007, Sharjah, United Arab Emirates.
8. R. Malekfar, **M. Mozaffari**, S. Mihanyar, *"The back scattering micro-Raman spectroscopy of different crystalline phases of* TiO_2 *nanoparticles produced by Sol-Gel technique*", Proceedings of 2nd International Spectroscopy Conference (AIP conference proceedings, Vol. 935, 120-125), Tunisian Physical Society (ISC2007), March 25-28 2007, Sousse, Tunisia.